ELSEVIER

J. Non-Newtonian Fluid Mech. xxx (2007) xxx–xxx

Journal of Non-Newtonian Fluid Mechanics

www.elsevier.com/locate/jnnfm

Role of the elasticity number in the entry flow of dilute polymer solutions in micro-fabricated contraction geometries

L.E. Rodd [a,b], J.J. Cooper-White [c,*], D.V. Boger [a], G.H. McKinley [b]

[a] *Department of Chemical and Biomolecular Engineering, The University of Melbourne, Australia*
[b] *Hatsopoulos Microfluids Laboratory, Department of Mechanical Engineering, Massachussets Institute of Technology, Cambridge, USA*
[c] *Department of Chemical Engineering, The University of Queensland, Brisbane, Australia*

Received 2 May 2006; received in revised form 7 February 2007; accepted 8 February 2007

Abstract

We explore the interplay of fluid inertia and fluid elasticity in planar entry flows by studying the flow of weakly elastic solutions through microfabricated planar contraction geometries. The small characteristic lengthscales make it possible to achieve a wide range of Weissenberg numbers ($0.4 < Wi < 42$) and Reynolds numbers ($0.03 < Re < 12$), allowing access to a large region of *Wi*–*Re* space that is typically unattainable in conventional macroscale entry flow experiments. Experiments are carried out using a series of dilute solutions ($0.78 < c/c^* < 1.09$) of a high molecular weight polyethylene oxide, in which the solvent viscosity is varied in order to achieve a range of elasticity numbers, $2.8 < El = Wi/Re < 68$. Fluorescent streak imaging and micro-particle image velocimetry (μ-PIV) are used to characterize the kinematics, which are classified into a number of flow regimes including Newtonian-like flow at low *Wi*, steady viscoelastic flow, unsteady diverging flow and vortex growth regimes. Progressive changes in the centreline velocity profile are used to identify each of the flow regimes and to map the resulting stability boundaries in *Wi*–*Re* space. The same flow transitions can also be detected through measurements of the enhanced pressure drop across the contraction/expansion which arise from fluid viscoelasticity. The results of this work have significant design implications for lab-on-a-chip devices, which commonly contain complex geometric features and transport complex fluids, such as those containing DNA or proteins. The results also illustrate the potential for using microfab-ricated devices as rheometric tools for measuring the extensional properties of weakly elastic fluids.

Keywords: Non-newtonian; Microfluidics; Particle image velocimetry; Contraction flow; Polyethylene oxide

1. Introduction

In macroscale devices (i.e. geometries in which the characteristic lengthscale is on the order of millimeters), it is essentially impossible to generate large deformation rates and correspondingly high Weissenberg numbers (*Wi*) in low viscosity elastic fluids, whilst also maintaining small Reynolds numbers (*Re*). As a result, it is difficult to induce an elastic response in which the effects of viscoelasticity are not dampened (or completely quashed) by the competing effects of fluid inertia. Microfluidic devices offer a solution by allowing high deformation rates and concomitantly low Reynolds numbers; a result that is directly attributable to the small lengthscale of the device.

Several recent studies have shown that the reduced lengthscales associated with microfluidic devices (on the order of tens to hundreds of microns) can enhance the magnitude of viscoelastic effects in dilute polymer solutions. This has been demonstrated in micro-fabricated converging or planar contraction geometries by Groisman and Quake [1] and in the recent work of Rodd et al. [2]. The same phenomena were also observed in the much earlier work of James and Saringer [3] at similar lengthscales and using similar aqueous solutions of flexible polymers. The importance of the device lengthscale and its effect on fluid elasticity is reflected in the definition of the elasticity number, $El = \lambda\eta/(\rho l^2)$, which is dependent only on fluid properties (relaxation time, solution viscosity, and fluid density) and the characteristic lengthscale of the device, *l*.

In addition to the unique flow conditions attainable by scaling down the geometry, microfluidic devices also offer the advantage of allowing access to a greater range of *Wi* and *Re*. This has been shown in our previous work [2], in which elasticity numbers spanning almost two orders of magnitude could be achieved. Accessibility to wide regions of *Wi*–*Re* space provides an avenue for generating suitable experimental data to test the performance

* Corresponding author. Tel. +61 7 33653661; fax: +61 7 33654199.
E-mail address: j.cooperwhite@uq.edu.au (J.J. Cooper-White).

0377-0257/$ – see front matter © 2007 Elsevier B.V. All rights reserved.
doi:10.1016/j.jnnfm.2007.02.006

of constitutive models over a wide range of flow conditions (with and without inertia). Furthermore, the ability of achieving high *Wi* at low *Re* offers the possibility of devloping microfluidic rheometers suitable for probing the rheological properties of weakly elastic fluids such as inks or dilute polymer solutions that appear Newtonian under the conditions that can be attained in conventional rheometers [2,4].

Very few experiments have been conducted specifically to test the effect of the elasticity number on complex viscoelastic flows, which is primarily attributed to the limited range of parameter space accessible through macro-scale experiments. With regards to planar contraction flows, the most thorough investigations of the effect of the elasticity number have been achieved through numerical simulations (see Table 1). We have previously provided a broader survey of experimental works in [2]; however in Table 1 we focus on planar flows which specifically investigate at least one of the following: (i) planar versus axisymmetric geometries, (ii) the effect of the elasticity number and (iii) the role of the viscoelastic Mach number, $Ma = \sqrt{Re\,Wi}$. In addition, many of the references in Table 1 also provide numerical predictions of the centreline velocity and/or extensional viscosity predictions.

To our knowledge, Rodd et al. [2] is the only experimental study which provides at least preliminary insight into the effect of *El* on the non-linear dynamics of planar entry flows. However, the range of values of the elasticity number in [2] was achieved by varying the polymer concentration, which is expected to lead to additional non-linear rheological effects associated with variable chain–chain interactions.

In the present work, we investigate the flow of four dilute polyethylene oxide solutions ($0.78 < c/c^* < 1.09$) through a microfabricated abrupt contraction–expansion geometry (contraction ratio, CR = 16), in which the smallest lengthscale of the device is 26 μm in the throat of the contraction. A range of elasticity numbers ($2.8 < El < 68$) are achieved by varying the solvent viscosity whilst maintaining a constant polymer concentration in solution ($c = 0.075$ wt.%). Experiments are performed over a range of flow conditions corresponding to $0.03 < Re < 12$ and $0.4 < Wi < 42$. Fluorescent streak imaging, micro-particle image velocimetry and pressure drop measurements are used to characterize the upstream flow kinematics associated with steady and time-dependent three-dimensional flow for both the elastic solutions and a Newtonian fluid, and to evaluate the extra pressure drop due to the elasticity of the solutions. Lastly, we assess the importance of the viscoelastic Mach number [5,6], and its role in determining the onset of diverging flow in this set of low viscosity elastic solutions.

1.1. Flow phenomena in viscoelastic entry flows

1.1.1. Planar versus axisymmetric geometries

It has been shown, both experimentally and numerically, that the kinematics associated with entry flows in planar and axisymmetric geometries are inherently quite different. For shear-thinning elastic fluids in planar contraction geometries, elastic corner vortices grow with increasing *Wi*; however the extent of vortex growth within a planar geometry [7–10] is less than in the equivalent axisymmetric geometry [11]. Table 1 identifies cases in which numerical simulations have been able to reproduce either qualitatively or quantitatively the results of specific experimental studies.

For Boger fluids however, vortex growth has not been observed in macro-scale planar contractions. Experimentally, Nigen and Walters [12] found (through both pressure drop measurements and streakline images) that for low to moderate flowrates, there is no discernable difference between the upstream flow dynamics in a Boger fluid and a Newtonian fluid in a 16 to 1 planar contraction. A number of 2D numerical simulations of flow through planar contractions for an Oldyroyd-B fluid [13,14] or an upper-convected Maxwell fluid [15–20], all lead to the same conclusion; the size of the corner vortex decreases with increasing Weissenberg number. However, higher values of *Wi* have been found to lead to the formation of unstable lip vortices. This has been observed both experimentally [12] and numerically [14,17].

The only case in which elastic corner vortex growth in Boger fluids has been observed in planar contractions has been in the recent experimental results of Rodd et al. [2]. In their work, micro-fabricated planar contractions were used in conjunction with a set of low viscosity Boger fluids in order to induce vortex growth, however this was only observed at moderate Reynolds numbers ($Re > 11$).

The reduced magnitude of elastic vortex growth that is observed experimentally in planar geometries, compared with their axisymmetric counterpart, is commonly attributed to the reduced strain rate in the geometry and/or the reduced total Hencky strain that is experienced by a polymer molecule as it flows through the contraction ($\epsilon_{axi} = 2\ln \mathrm{CR}$, compared with $\epsilon_{planar} = \ln \mathrm{CR}$) [21]. However, even for high contraction ratios, non-linearities in the dynamic response have been found to be virtually absent in planar geometries [22]. Changing the contraction ratio by adjusting the upstream channel width results in an increase in the total Hencky strain however this extra contribution only occurs in the upstream tail of the strain rate profile, i.e. regions in which the strain rate is typically small and less than the critical value, $\dot{\epsilon}_{crit} = 1/\lambda$, required for polymer extension. As a result, the Hencky strain that is accumulated in high strain rate regions that actually lead to chain extension remains unchanged [22]. It is therefore the non-homogeneity of the strain rate profile observed in planar contraction flows that is considered responsible for the lack of non-linearity in the stress-response. This observation was made by Genieser et al. based on birefringence measurements in Boger fluids and 1D predictions using the Geisekus model, and the upper-convected and linear Maxwell models [22]. Their arguments however, do not explain off-centreline dynamics, such as the sustained vortex growth observed in shear-thinning viscoelastic fluids.

Quinzani et al. also made point-wise flow-induced birefringence measurements in a shear-thinning viscoelastic fluid flowing through a 4:1 planar contraction [23,24]. Although they quantify in great detail the fluid velocity, shear stress and first normal stress difference as a function of spatial position, their measurements were only carried out in a planar geometry, precluding any direct comparison of the corresponding extensional stresses induced in planar and axisymmetric geometries for the

Please cite this article in press as: L.E. Rodd et al., Role of the elasticity number in the entry flow of dilute polymer solutions in micro-fabricated contraction geometries, J. Non-Newtonian Fluid Mech. (2007), doi:10.1016/j.jnnfm.2007.02.006

Table 1
Review of previous entry flow studies in axisymmetric (A), planar (P), and square (S) geometries: an addendum to Table 1 of Rodd et al. 2005 [2]

Author	Year	Exp., num.	Planar, axisymmetric, square	2D, 3D	Aspect ratio, $\Lambda_u = h/w_u$	Contraction ratio, CR	Fluid	Rheology	*Wi* range	*Re* range	Comments
Genieser et al.	2003	E, N	P	2D	1	8.32	Boger fluid, 0.3% PIB/PB Giesekus fluid UCM fluid	Giesekus model, UCM model	$0 < Wi < 2.9$	Unknown	For CR = 8, effects of elasticity in dimensionless strain rate profile observed for $Wi > 2$ Three-dimensional effects observed at $Wi > 2.3$ (CR = 8) and $Wi > 3.1$ (CR = 32). For both CR = 8 and 32, negligible non-linear effects in η_E observed for all $0 < Wi < 3.1$, for total Hencky strains $\varepsilon = 3.5$; attributed to non-homogenous strain rate profile, slow response of long relaxation time modes, and contribution of solvent viscosity η_E
Quinzani et al.	1995	E	P	3D	10	4	5% PIB in tetradecane	ψ_1, η	$0.25 < Wi < 0.77$	$0.08 < Re < 1.43$	Flow-induced birefringence (FIB) measurements indicate a peak in the transient extensional viscosity along centreline that decreases with increasing *Wi*. No flow visualisation
Quinzani et al.	1994	E	P	2D	10	3.91	5% PIB in tetradecane	ψ_1, η, η', η'', λ determined using UCM (upper-convected Maxwell) model	$0.25 < Wi < 0.77$ (shear-rate dep.) $0.4 < Wi_0 < 4.15$ (zero-shear)	$0.08 < Re < 1.43$ (shear-rate dep.) $0.08 < Re_0 < 0.8$ (zero-shear)	Laser doppler velocimetry (LDV) and FIB used to measure axial velocity, shear stress and first normal stress difference (axial and radial). Maximum in centreline N_1 and τ_{xy} in lateral profile increases with *Wi*. Small overshoot in axial velocity observed just downstream of contraction for mod. to high *Wi*
Kim et al.	2005	N	P	2D	–	4	Oldroyd-B fluid with $\eta_s/\eta_0 = 1/9$	Oldroyd-B model	$0 < Wi < 5$	$Re = 0, 0.1$	For $Re = 0$, vortex size reduces, lip vortex increases with increasing *Wi*. Lip vortex intensity a strong function of mesh refinement. Agreement with Alves et al. (2003) in both vortex size and intensity. Predicts 'delayed' acceleration at centreline in region nearest contraction plane. Accompanied by overshoot in V_z
Webster	2004	N	P	2D	–	4	Oldroyd-B fluid with $\eta_s/\eta_0 = 1/9$	Oldroyd-B model	$Wi = 0.3, 2$	$Re = 0$	Start-up flows with transient/static inlet boundary conditions. Steady state vortex size is unchanged with higher *Wi*; effect of higher *Wi* is to increase the time taken to reach steady state, and intermediate vortex size in approaching steady state

Please cite this article in press as: L.E. Rodd et al., Role of the elasticity number in the entry flow of dilute polymer solutions in micro-fabricated contraction geometries, J. Non-Newtonian Fluid Mech. (2007), doi:10.1016/j.jnnfm.2007.02.006

Table 1 (*Continued*)

Author	Year	Exp, num.	Planar, axisymmetric, square	2D, 3D	Aspect ratio, $\Lambda_u = h/w_u$	Contraction ratio, CR	Fluid	Rheology	*Wi* range	*Re* range	Comments
Aboubacar et al.	2002	N	A, P	2D	–	4	PTT fluid with $\varepsilon = 0.02$, 0.25 and $\eta_s/\eta_0 = 1/9$ Oldroyd-B model	4 variants of PTT and Oldroyd-B models	$0 < Wi < 35$	$Re = 0$	Oldroyd-B, planar: vortex size reduction with increasing *Wi*. PTT with $\varepsilon = 0.25$, 0.02: vortex growth, followed by a vortex reduction at higher *Wi*. Delayed (higher *Wi*) onset of vortex reduction for higher values of ε
Moatssime	2001	N	P	2D	–	4	Oldroyd-B fluid with η_s/η_0 unspecified	Oldroyd-B model	$1 < Wi < 4.5$	$Re = 0.1$	Upstream behaviour in the first normal stress difference not distinguishable for $1.5 < Wi < 4.5$. Higher *Wi* increases peak value in ψ_1 at contraction plane and leads to longer downstream recovery
Ryssel and Brunn	1999	N	P	2D	–	4	Quasi-Newtonian Giesekus fluid	Geisekus and quasi-Newtonian model	$Wi = 1.45$	$Re = 0.56$	Results for QNF agree qualitatively with those of Quinzani, in terms of axial and lateral velocity profiles, shear stress and first normal stress profiles. Velocity overshoot predicted by the Giesekus model is not predicted for QNF (agrees with experiment)
Xue et al.	1998 (i)	N	P	2D and 3D	0.5–5	4	PTT fluid with $\varepsilon = 0.02$, 0.25 and $\eta_s/\eta_0 = 0$ Oldroyd-B and UCM fluid	UCM, PTT, Oldroyd-B models	$0 < Wi < 4.4$	$0.06 < Re < 0.6$	Vortex growth at small $Re = 0.06$ for increasing *Wi*. For higher $Re > 0.5$ size of vortex overpredicted by creeping assumption for both Newtonian and viscoelastic. For constant $Re > 0$, size of salient corner vortex is constant for increasing *Wi*. Vortex mechanisms dependent on elasticity (*El*) and Mach (*Ma*) numbers. 2D approximation valid for upstream ratio $\Lambda_u = h/w_u > 5$
Xue et al.	1998 (ii)	N	P, S	2D and 3D	–	4	PTT fluid with $\varepsilon = 0.25$ and $\eta_s/\eta_0 = 1/9$. UCM fluid with $\lambda = 0.8$ s	Simplified PTT model, UCM model	$0 < Wi < 7.2$	$0.01 < Re < 0.1$	Vortex growth observed for UCM fluid in square-square contraction and not planar. For PTT fluid, vortex growth occurs in the planar geometry although to a lesser degree than in axisymmetric. Peak in the predicted transient extensional viscosity along the centreline for PTT less than for a Newtonian fluid.

Please cite this article in press as: L.E. Rodd et al., Role of the elasticity number in the entry flow of dilute polymer solutions in micro-fabricated contraction geometries, J. Non-Newtonian Fluid Mech. (2007), doi:10.1016/j.jnnfm.2007.02.006

Mompean	1997	N	P	2D and 3D	10	4	Oldroyd-B fluid with $\eta_s/\eta_0 = 1/9$	Oldroyd-B model	$0 < Wi < 27.3$	$0 < Re < 0.138$	For both Newtonian and viscoelastic, vortex size reduces with increasing *Re* (Newtonian) or increasing *Wi* and *Re* (non-Newtonian). Good agreement between experimental (Quinzani et al. [25]) and predicted lateral velocity profiles (V_z vs. x), at various upstream locations $-0.25 < (z/w_c) < 2.5$. Predictions of first normal stress fail in regions near the contraction
Hulsen	1993	N	A	2D	–	4	PTT fluid, $\varepsilon = 0.25$ and $\varepsilon = 0.02, \eta_s/\eta_0 = 1/6$	PTT model	$1 < Wi < 16$	$0 < Re < 10$	Vortex growth with increasing *Wi* for $Re = 0$. For $Re > 0$, vortex size function of El. The presence of diverging streamlines dependent on El, *Ma* and the extensionability parameters. For $\varepsilon = 0.02$. Diverging flow not observed for $\varepsilon = 0.25$

same fluid. Raiford and co-authors explored the flow of the same shear-thinning fluid in an axisymmetric contraction, however they only quantified the velocity field.

1.1.2. Interplay of fluid inertia and fluid elasticity: effect of the elasticity number and the viscoelastic Mach number

The relative magnitudes of fluid elasticity and fluid inertia may be expressed in terms of the elasticity number, $El = Wi/Re$. For a given experiment in which the geometry is fixed, the elasticity number is therefore the slope of the trajectory in *Wi*–*Re* space that represents a series of step flow-rate experiments. An example of this representation of previous entry flow experiments may be found in [2], in which the various flow regimes have been illustrated as a phase diagram in *Wi*–*Re* space. In cases for which the fluid properties (relaxation time and fluid viscosity) are independent of shear-rate, the elasticity number is constant and experiments are represented by lines of constant slope in *Wi*–*Re* space. An alternative representation of entry flow experiments in which both fluid inertia and fluid elasticity are significant can be developed in terms of the viscoelastic Mach number, $Ma = \sqrt{Wi\,Re}$. The Mach number is the ratio of the local velocity, v to the speed of a viscoelastic shear wave, $c_s = \sqrt{G/\rho} = \sqrt{\eta_p/\rho\lambda}$. Here, G is the elastic modulus of the fluid, which for a Maxwell body may also be defined as η_p/λ. The definition of *Ma* therefore shows that it is only possible to induce viscoelastic shear waves if both $Re \neq 0$ and $Wi \neq 0$. Consequently, the results of numerical simulations which utilize non-zero values of *Wi* and *Re* are inherently different from those in which either $Wi = 0$ or $Re = 0$. Hulsen [5] proposes that the onset of diverging flow corresponds to a transition from elliptic vorticity transport (sub-critical) to hyperbolic vorticity transport (super-critical), which occurs at $Ma = 1$. By analogy to a phase diagram of flow regimes in *Wi*–*Re* space, an equivalent representation of previous studies of viscoelastic flows through contractions may also be constructed in *El*–*Ma* space [20]. However, an advantage of utilizing the *Wi*–*Re* co-ordinate system is that there exists a well-defined Newtonian flow limit at $Wi = 0$. There is no equivalent limit in *El*–*Ma* space which corresponds exclusively to Newtonian flow.

As noted earlier, the influence of the elasticity number on planar entry flows has been explored almost exclusively through numerical simulations, as summarized in the present work in Table 1, and in Table 1 of [2]. For both Newtonian and viscoelastic entry flows, an increase in Reynolds number results in a reduction in vortex size. However, this “inertial” suppression of the upstream corner vortex often relies on the cooperative effects of fluid elasticity. For example, Kim et al. [14] found that an increase in the Reynolds number from $Re = 0$ to $Re = 0.1$ had no effect on the vortex length in a Newtonian fluid. For an Oldroyd-B fluid, the same change in Reynolds number leads to a clear reduction in vortex size. The interplay of inertia and elasticity demonstrated by this calculation has been observed in several viscoelastic flows in which the Reynolds number is small (i.e. $Re \ll 1$), but non-zero. An example of this includes the presence of diverging streamlines, which have been observed experimentally in the entry flow of Boger fluids, at Reynolds numbers less than 0.1 [25,26], and more commonly in shear-thinning elastic fluids [7–11,27,28]. In the latter case, inertia has always been present due to the shear-thinning nature of the fluids. As discussed in [2], diverging streamlines are identified as those which locally diverge away from the centreline immediately upstream of the contraction plane, prior to converging again as the flow enters the contraction throat. They are considered a signature feature of contraction flows in which both inertia and elasticity are important.

For sufficiently high elasticity numbers, an increase in Reynolds number can simultaneously lead to the growth of lip vortices. However, it is argued by Xue et al. [19], that the presence of the lip vortex is not a result of fluid inertia, but relies more on small, but non-zero, values of the relevant non-linear constitutive parameter (in the case of [19], the fluid is described by the PTT model and the parameter $\epsilon = 0.02$). In addition, the presence of lip vortices is also dependent on mesh refinement, which has been the cause of discrepancies in the predicted lip vortex dynamics that have been reported by different numerical studies. Several other computational works investigating the effect of inertia on planar entry flows of shear-thinning fluids (PTT, FENE-P) [13,14,19,20,29] and Boger fluids (Oldroyd-B, UCM) fluids [15,16,19,20] are detailed in Table 1.

Hulsen [5] and Joseph [6] have previously discussed the relevance of the vis-coelastic Mach number, $Ma = v/c$, and its application to viscoelastic entry flows. For the most elastic fluid considered in Hulsen's calculations [5], the onset of diverging flow corresponds to conditions in which regions of $Ma > 1$ extend upstream of the contraction plane in a circular geometry. However, this criterion did not appear to hold for higher values of ϵ (lower fluid elasticity). For a PTT fluid with $\epsilon = 0.25$, diverging streamlines did not develop over the entire range of flow conditions tested, despite the large regions of $Ma > 1$ that exist at higher flowrates. Hulsen [5] therefore suggested that the vis-coelastic Mach number cannot be the only parameter important in determining the onset of diverging flow. Xue et al. [20] also emphasize the importance of both the Mach number and the elasticity number, and present a phase diagram of vortex mechanisms in terms of *El–Ma* space. Their phase diagram indicates the requirement of a high elasticity number and at least moderate values of the Mach number in order to generate upstream corner vortices. In their work [20], unstable flow was observed at high elasticity numbers and high Mach numbers.

2. Experimental

2.1. Channel geometry and fabrication

In Fig. 1 we show a schematic of the microdevice used in the present experiments. The dimensions of the planar 16:1:16 contraction–expansion geometry are very similar to those used in our previous work [2], with an upstream channel width, w_u, of 400 μm, a contraction throat width, w_c, of 26 μm and a uniform channel depth, h of 55 μm. Channels are fabricated in PDMS using standard soft-lithography techniques and SU-8 photolithography. Further details of the fabrication procedure may be found in [2,30].

In contrast to [2], in the present work PDMS channels are bonded to PDMS-covered glass coverslips in order to achieve uniform surface properties on all four walls of the channels. PDMS is spin-coated onto the glass coverslip using a spin speed of 3000 rpm to achieve a ~20 μm-thick layer of PDMS. The different ratios of PDMS to curing agent (CA) between the channel (PDMS:CA = 5) and the coverslip (PDMS:CA = 10) ensure that the seal between the two surfaces is able to withstand pressures

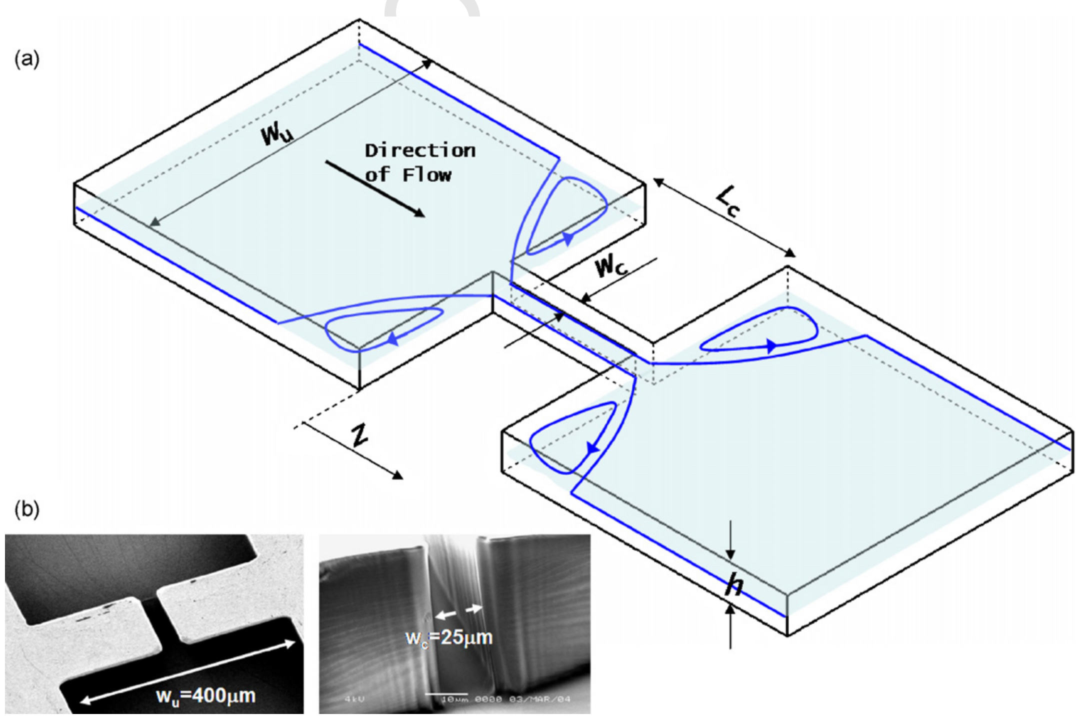

Fig. 1.

Please cite this article in press as: L.E. Rodd et al., Role of the elasticity number in the entry flow of dilute polymer solutions in micro-fabricated contraction geometries, J. Non-Newtonian Fluid Mech. (2007), doi:10.1016/j.jnnfm.2007.02.006

Table 2
Solution properties and experimental parameters

	Glycerol in solvent (wt.%)			
	15	30	45	60
η_s (mPa s)	1.56	2.61	4.68	10.6
η_0 (mPa s)	2.96	4.79	9.03	17.3
η_p (mPa s)	1.40	2.18	4.35	6.76
ρ (kg/m^3)	1073	1112	1153	1196
λ_{CaBER} (ms)	8.3	10.3	17.2	20.8
λ_{Zimm} (ms)	0.542	0.869	1.34	2.31
$[\eta]$ (ml/g)	924	886	763	582
R_g (nm)	202	199	189	173
$\dot{\gamma}_c$ (s^{-1})	750–56,800	750–37,400	750–32,900	750–23,800
Re	0.14–11.5	0.09–5.1	0.05–2.0	0.03–0.6
Wi	0.4–32	0.65–36	1–38	1.7–42
El	2.8	7.0	19	68

in excess of 180 kPa. Bonding is achieved by placing the two surfaces together after 20 min of baking at 80 °C, and then baking the sealed channel at 80 °C for a further 24 h.

Pressure taps are located 3 mm upstream and 3 mm downstream of the contraction midpoint. The volumetric flowrate is controlled via a precision syringe pump (Harvard Apparatus PHD2000), in order to achieve a range of flowrates, 0.01 ml/h < Q < 9 ml/h. These correspond to characteristic deformation rates of $149\,\mathrm{s}^{-1} < \dot{\gamma}_c = 2Q/(w_c^2 \times h) < 1.35 \times 10^5\,\mathrm{s}^{-1}$ in the contraction throat (where Q is the volumetric flowrate, w_c the contraction width and h is the uniform depth of the channel). Further details of the pressure measurement setup, transducer calibration and data acquisition can be found in [2,30].

2.2. *Fluid rheology*

2.2.1. *Relaxation times*

Four aqueous solutions containing 0.075 wt.% of a weakly polydisperse sample of high molecular weight polyethylene oxide (PEO, $M_W = 2 \times 10^6$ g/mol, polydispersity index = 1.13, Aldrich) were prepared using mixtures of water and increasing amounts of glycerol (15, 30, 45 and 60 wt.%) as the solvent. For brevity, we hereafter denote the four polymer solutions by P15G, P30G, P45G, and P60G, for the PEO solutions containing 15, 30, 45 and 60% glycerol, respectively. The rheological properties for each of these solutions are given in Table 2. All solution properties were measured at 23 °C.

Characteristic relaxation times for each of the four solutions were calculated according to Zimm theory (as was done in our previous work [2]), and were also measured using capillary breakup extensional rheometry (CaBER) [31]. The geometrical configuration of the CaBER device employed in the present experiments was similar to that used in [2] ($\Lambda = 1.57$, $h_0 = 2.5$ mm). The measured relaxation times were found to have a range of 4 ms < λ < 40 ms.

The Zimm relaxation time is calculated from an expression of the form

$$\lambda_{\mathrm{Zimm}} = F\frac{[\eta]M_W\eta_s}{N_A k_B T} \tag{1}$$

where M_W is the molecular weight, N_A the Avogadro's constant, k_B the Boltzmann's constant, T the absolute temperature, η_s the solvent viscosity, and $[\eta]$ is the intrinsic viscosity. The prefactor, F may be estimated by the Riemann Zeta function, $\zeta(3\nu)^{-1} = \sum_{i=1}^{\infty} 1/i^{3\nu}$ in which ν is the solvent quality exponent [32].

Values of the intrinsic viscosity used in the above expression were obtained from U-tube capillary viscometer measurements and were found to be a strong function of the mass fraction of glycerol in solution. This is illustrated in Fig. 2, in which the intrinsic viscosity decreases from 1026 to 582 ml/g as the glycerol content is increased from 0 to 60 wt.%. This suggests that the thermodynamic solvent quality, ν, reduces as the glycerol content is increased, resulting in a progressive collapse in the dimensions of the unperturbed polymer coil. A measure of the change in polymer coil size as a function of intrinsic viscosity can be approximated according to the Fox–Flory equation [33], for which values are given in Table 2.

The value of the solvent quality, ν, could not be determined for each solution of varying glycerol content due to the lack of available experimental data regarding the influence of glycerol content on the parameters in the Mark–Houwink correlation for PEO. The front factor $F = 0.463$ was therefore calculated for a good solvent ($\nu = 0.55$), which in combination

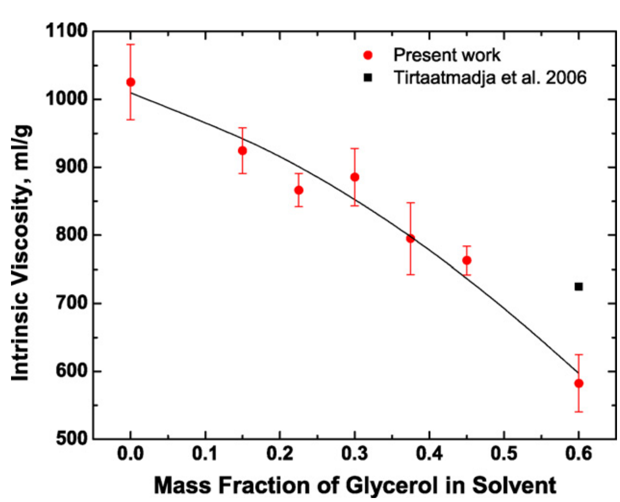

Fig. 2.

Please cite this article in press as: L.E. Rodd et al., Role of the elasticity number in the entry flow of dilute polymer solutions in micro-fabricated contraction geometries, J. Non-Newtonian Fluid Mech. (2007), doi:10.1016/j.jnnfm.2007.02.006

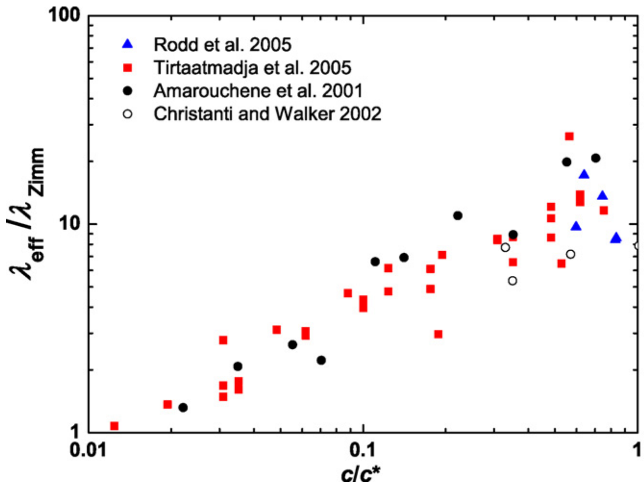

Fig. 3.

with the measured intrinsic viscosity data, was used to calculate Zimm times for each of the PEO solutions, $\lambda_{Zimm}=0.54$, 0.87, 1.34, and 2.31 ms, in order of increasing glycerol content.

In Fig. 3, our measured values of the effective fluid relaxation time measured in elongational flow using the CaBER device are presented on a master plot of $\lambda_{eff}/\lambda_{Zimm}$ versus c/c^* for a number of aqueous PEO solutions [32]. The values of $\lambda_{eff}/\lambda_{Zimm}\sim 10$–20 for the present solutions were found to agree with those obtained from various drop breakup [32,34] and jetting experiments [35]. This agreement is expected as, in all cases, the characteristic relaxation time is extracted from the filament dynamics associated with the strong transient flow of a low-viscosity polymer solution undergoing elasto-capillary thinning. However, the large discrepancy between the calculated Zimm times and the measured CaBER relaxation times suggests that the imposed flow field during CaBER measurements is significantly affecting the polymer chain dynamics and/or the theoretical analysis of the thinning dynamics is overly simplified [36,37].

In order to avoid any confusion regarding relaxation times throughout this work, we will use the Zimm relaxation time in all following discussions and Weissenberg number calculations, and this will be denoted generically by λ. Our justification for this choice is as follows: firstly, the Zimm time is generally of the same order of magnitude as the timescales obtained by fitting constitutive models, such as the Oldroyd-B model to viscosity and first normal stress difference data obtained in steady shear [38]. Numerical simulations using these models can only be expected to predict the results of the present experiments if the computed material functions for the constitutive model are close to those measured in the fluid. The increase in λ_{eff} during transient elongation that is shown in Fig. 3 must therefore be predicted from the constitutive theory. Although current closed form theories for polymer solutions do not show such increases, recent Brownian dynamics calculations with bead-spring chains in planar elongation do show a similar concentration-dependence in the longest relaxation time [39]. Similarly, the results of the present experiments may only be compared with those of previous macroscale experiments (in which the fluid rheology is often well-described by constitutive models such as the Oldroyd-B model) if comparable definitions of timescales are used.

2.2.2. *Steady shear viscosity*

The steady shear viscosity of all polymer solutions and their solvents was measured using a stress-controlled rheometer (AR2000) using a double-gap Couette cell attachment. The viscosities of each of the solutions were found to be constant over the range of shear rates, $2\,s^{-1} < \dot{\gamma} < 3000\,s^{-1}$, with values ranging from 3 to 17 mPa s (Table 2). The density of the four PEO solutions was measured using calibrated 5 ml density flasks at 23 °C. The density of the solutions increased linearly with mass fraction of glycerol, and as a result, PEO concentrations (when expressed in units of g/ml) vary between 8.05×10^{-4} and 8.97×10^{-4} g/ml. These values of concentration are used to determine values of c/c^*, in order to maintain consistency with the units for $[\eta]$, ml/g.

Since the microfluidic geometry is the same for all measurements presented in this work, the elasticity number, $El=\eta_0\lambda/\rho l^2$ only varies due to changes in the relaxation time, the solution viscosity and less significantly, by the density. The four solutions containing solvents 15, 30, 45 and 60% glycerol in water, correspond to elasticity numbers $El=3.8, 7.1, 19$, and 68, respectively, using a constant lengthscale, $w_c = 26\,\mu m$, the Zimm relaxation time and the measured solution properties presented in Table 2. In our previous work [2], we used the same geometry and three solutions of various elasticity numbers, $El=8.4$, 3.8 and 89, which were all calculated using the *CaBER-determined* relaxation times. For the purpose of comparison only, if the elasticity numbers for the present experiments are re-calculated based on their CaBER-determined relaxation times, these values are $El=43$, 84, 240 and 610 for the P15G, P30G, P45G and P60G solutions, respectively; i.e. an order of magnitude higher than those used in [2].

2.2.3. *Flow visualisation*

The upstream kinematics associated with the flow of deionized water and all PEO solutions through the 16:1 contraction were visualized using fluorescent streak imaging and micro-particle image velocimetry (μ-PIV). A schematic of the geometry and the imaging setup are detailed in Fig. 4.

In order to generate streak images, fluids were seeded with 1.1 μm epi-fluorescent particles (Ex./Em. = 520/580 nm, $c=0.02$ wt.%), and exposed to a continuous illumination Mercury lamp. Further details on the streak imaging setup may be found in [2]. As in our previous work [2], the measurement depth, δz_m [40] is chosen as the appropriate lengthscale to represent the depth of the image plane on which streak lines are observed. For our streak imaging setup ($M=10\times$, NA = 0.3), the measurement depth was found to be $\delta z_m=33.6$, which is 60% of the channel depth.

PIV image pairs were acquired using a SensicamQE double-frame camera in conjunction with a double-pulsed 532 nm Nd:YAG laser, in which the exposure time of each image is set

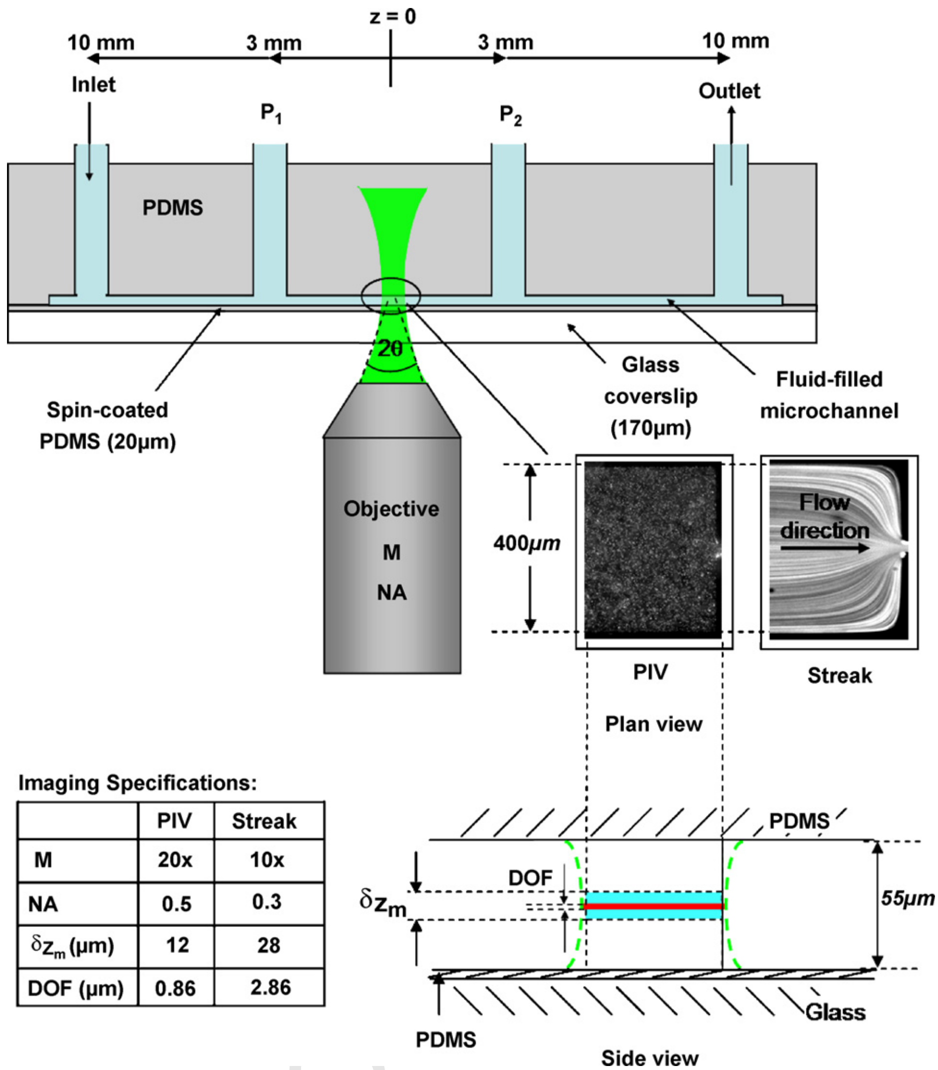

Fig. 4.

by the pulse width, $\delta t = 5$ ns. Images of 0.51 μm epi-fluorescent particles were acquired through a 20× (NA = 0.5) objective lens, for which the resulting measurement depth is 12 μm; this is equivalent to 21% of the channel depth. The majority of PIV images (apart from those used to generate the out-of-plane velocity profile in Fig. 6b) were acquired at the centreplane ($y = 0$), which was identified as the midpoint of two stationary fluorescent particles adhered to the top and bottom surfaces of the microchannel. The uncertainty of the centreplane position (and out-of-plane position) is therefore a function of the uncertainty of locating an individual particle (i.e. DOF = 0.86 μm), the size of the particle ($d_p = 0.5$ μm), and the size of a division on the microscope focussing micrometer; error values were calculated to be $\epsilon_y = \pm 2$ μm and are represented by horizontal error bars in Fig. 6b.

The time between individual PIV images, Δt, was set in order to achieve an optimum particle displacement ($2d_p < \Delta x < 7.5d_p$, in which d_p is the particle diameter) [40,41] between images at all positions along the centreline. To accommodate regions of higher velocities nearer the contraction, a second set of images were acquired using a smaller value of Δt; one quarter of the value used for regions further upstream. The time between laser pulses, Δt was therefore adjusted over the range (19 μs < Δt < 634 μs) according to the flowrate and region of interest (i.e. the local velocity).

A conventional cross-correlation PIV algorithm (TSI Insight, http://www.tsi.com) was used to analyze each image pair. Interrogation areas of 32 × 32 and 16 × 16 pixels (with Nyquist criterion) were used to generate full field velocity maps. Further details on PIV processing algorithms and optimization guidelines can be found elsewhere [40,30]. Two modes of PIV image processing were utilized during experiments. The first mode was used only for steady flows in which 25 image pairs were ensemble-averaged to obtain a single vector field. The second mode was used for unstable flows, in which only one pair of images was used to characterize the flow at a particular instant in time. Post-processing techniques to remove spurious vectors and to interpolate for missing vectors were only applied in regions upstream of the contraction ($z/w_c < -5$), i.e. where velocity gradients are relatively small.

Please cite this article in press as: L.E. Rodd et al., Role of the elasticity number in the entry flow of dilute polymer solutions in micro-fabricated contraction geometries, J. Non-Newtonian Fluid Mech. (2007), doi:10.1016/j.jnnfm.2007.02.006

2.3. Dimensionless groups

Four dimensionless quantities are used to characterize the dynamics of the flow of the polymer solutions through the 16:1 contraction geometry: the Weissenberg number (*Wi*), Reynolds number (*Re*), elasticity number (*El*) and the viscoelastic Mach number (*Ma*). The following definitions for *Wi, Re* and *El* were also used in our previous work [2], and for consistency, we follow the same notation and definitions. The Weissenberg number is defined in terms of a characteristic polymer relaxation time and the average shear rate in the contraction throat:

$$Wi = \lambda\dot{\gamma}_c = \frac{\lambda \bar{V}_c}{w_c/2} = \frac{\lambda Q}{h w_c^2/2}, \tag{2}$$

in which $\bar{V}_c = Q/(w_c h)$ is the average velocity, w_c the contraction width, h the depth of the channel, Q the volumetric flowrate, and λ is the Zimm relaxation time.

The Reynolds number is defined in terms of the average velocity in the contraction throat, $\bar{V}_c$, and the hydraulic diameter, D_h, which is given by $D_h = 2w_c h/(w_c + h)$:

$$Re = \frac{\rho \bar{V}_c D_h}{\eta_0} = \frac{2\rho Q}{(w_c + h)\eta_0}, \tag{3}$$

where the fluid density is denoted by ρ. Although we have chosen η_0 as the characteristic viscosity in the above expression, the weak variation of the shear viscosity of dilute polymer solutions, and the relative magnitudes of the zero-shear and infinite-shear viscosities for all solutions (Table 2) indicate that the choice of characteristic viscosity (i.e. zero-shear, infinite-shear, or a local shear-rate dependent) would have minimal effect on both the relative values and magnitude of *Re* for all flow conditions.

The elasticity number represents the ratio of elastic to inertial stresses, and is independent of kinematics. It is only dependent on the properties of the fluid and on the characteristic length-scales of the device, h and w_c:

$$El = \frac{Wi}{Re} = \frac{\lambda\eta}{\rho w_c D_h} = \frac{\lambda\eta(w_c + h)}{2\rho w_c^2 h} \tag{4}$$

The viscoelastic Mach number, $Ma = V/c$, is the ratio of a characteristic velocity, V to the viscoelastic wave speed, $c_s = \sqrt{G/\rho}$, where $G = \eta_p/\lambda$ is the elastic modulus of the fluid and η_p is the polymer contribution to the zero-shear viscosity.

As described in Section 1.1.2, the magnitude of the viscoelastic Mach number can be used to identify regions of elliptic ($Ma < 1$) and hyperbolic ($Ma > 1$) vorticity transport. This is the case for a Maxwell type fluid in which the solvent viscosity $\eta_s = 0$, and true hyperbolicity is phenomenologically not possible when a Newtonian solvent is present; the viscous contribution to the stress results in a dispersion of the shear waves. However, when $\eta_p/\eta_s \gg 1$ or $\eta_E/\eta_s \gg 1$ the elastic stresses are much greater than the viscous stresses and very similar phenomena may occur. This has been documented by Hulsen [5] who simulated the circular entry flow for an Oldroyd-type fluid in which $\eta_0/\eta_s = 6$. In the present work, the local viscoelastic Mach number $|\underline{v}(x, y)|/c$ is evaluated throughout each complex flow using the PIV-determined velocity field. For the solutions used in the present work, $\eta_p/\eta_s \sim O(1)$. Furthermore, pressure drop measurements in Section 3.3 suggest that for the most elastic solution $\lim_{\dot{\epsilon}\to\infty}\eta_E/\eta_s < 10$. The low values of η_p/η_s may therefore lead to a condition in which $Ma > 1$ is not an exact criterion for determining regions of hyperbolic vorticity transport. However, comparing the relative magnitude of the local viscoelastic Mach number between individual experiments may still be expected to be qualitatively meaningful.

The dimensionless pressure, $\Delta\mathcal{P}$ is obtained by normalising the differential pressure $\Delta P_{12} = P_1 - P_2$ by the linear slope of the pressure drop/flowrate curve that is observed in all experiments at low *De* [12]. Hence, $\Delta\mathcal{P}(Re, De) = \Delta P_{12}/(sQ)$, where $s = \mathrm{d}\Delta P_{12}/\mathrm{d}Q$ when $Q \to 0$. This procedure is identical to that followed in [2].

3. Results

3.1. Streak imaging

Streak images of each of the four solutions were used to identify the onset of "steady viscoelastic flow" at Weissenberg numbers of ($Wi \cong 3$–4) for the three lower elasticity number solutions ($El = 2.8$, 7, and 19). In this flow regime, converging streak lines exhibit an inflection upstream of the contraction plane, such as those illustrated in Fig. 5d. This is in contrast to Newtonian flows, in which the converging streak lines only experience an inflection upon entering the contraction. For the most elastic solution, P60G ($El = 68$) the transition from Newtonian-like to steady viscoelastic flow occurs at a higher Weissenberg number, $Wi \cong 10$.

Streak images for all solutions at $Wi \cong 10$–11 are presented in Fig. 5. For $El = 2.8$, 7 and 19, this corresponds to the "diverging flow" regime. Pronounced additional streamline curvature can be observed upstream of the contraction plane. Again, the transition to diverging flow for the most elastic solution, $El = 68$ occurs at a higher Weissenberg number, $Wi \cong 17$–20. At $Wi \cong 17$, the flow of the other three solutions becomes three-dimensional, unstable and time-dependent.

In unsteady flows, it is difficult to characterize the vortex mechanism using streak image analysis, due to the high frequency of oscillations in the flow structure and the three dimensional nature of the flow. PIV partly resolves these difficulties, firstly by capturing an image of the flow field over a small time interval ($1 < \mathrm{d}t < O(10^2)$ μs) to achieve instantaneous vector maps, and secondly, by interrogating a smaller measurement depth (δz_m) by using a higher numerical aperture objective. Analysis of flow structures within the diverging and unstable flow regimes will therefore be addressed in the following sections.

3.2. Micro-particle image velocimetry

3.2.1. Experimental validation: Newtonian flow in a rectangular channel

In order to quantify the velocity field associated with the complex flow through a planar contraction, it is first necessary to confirm that the combined measurement and analysis tech-

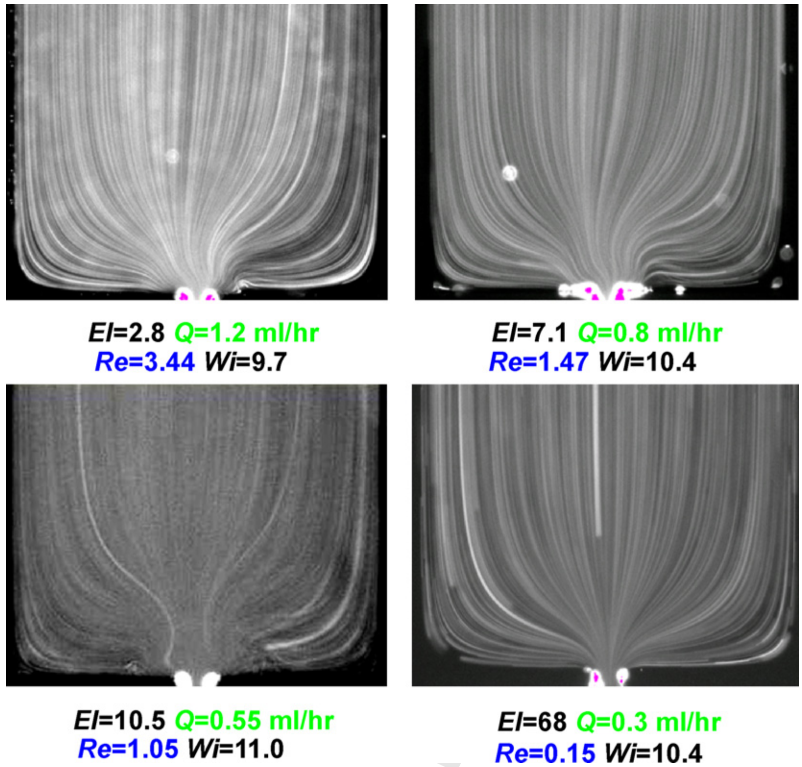

Fig. 5.

nique yields correct values of the velocity. This was achieved by conducting PIV measurements in a section of the PDMS channel in which the flow is rectilinear (i.e. far upstream of the contraction). Velocities were measured in both the x–y planes and x–z planes in order to construct the three-dimensional velocity profile, which was then compared with the analytical solution for Poiseuille flow in a channel of rectangular cross-section. In the present geometry, x is in the direction of the channel width, y is in the direction of the channel depth, and z is in the direction of the flow.

Eq. (5) represents the z-component of the dimensionless Navier–Stokes equations, in which $v_z' = v_z/\langle v_z\rangle_u$ is the dimensionless axial velocity, and $\xi = x/(w_u/2)$ and $\nu = y/(h/2)$ are the dimensionless x and y positions, respectively. For viscous flows, it is customary to normalize the pressure gradient with the viscous pressure, $P_{visc} = \mu\langle v_z\rangle_u/(h/2)^2$, such that the dimensionless pressure drop is given by $\Delta\mathcal{P} = (\mathrm{d}P/\mathrm{d}z)/P_{visc}$.

$$\frac{1}{\alpha^2}\frac{\partial^2 v_z'}{\partial\xi^2} + \frac{\partial^2 v_z'}{\partial\nu^2} = \Delta\mathcal{P} \quad (5)$$

Use of Eq. (6) below as the general form of the solution for v_z' reduces Eq. (5) to a Laplace equation, which can then be solved easily using the method of ‘separation of variables’ with homogenous boundary conditions, $v_z' = 0$ at $\nu = \pm 1$ and $\xi = \pm 1$, $\partial v_z'/\partial\xi = 0$ at $\xi = 0$, and $\partial v_z'/\partial\nu = 0$ at $\nu = 0$.

$$v_z'(\xi,\nu) = X(\xi)Y(\nu) + \Delta\mathcal{P}(\nu) \quad (6)$$

The resulting solution to the axial velocity in a rectangular channel is given by [42]:

$$v_z' = \frac{\sum_{n=0}^{\infty}((-1)^n/\sigma_n^3)\cos(\sigma_n\nu)[1-(\cosh(\sigma_n\alpha\xi)/\cosh(\sigma_n\alpha))]}{\sum_{n=0}^{\infty}(1/\sigma_n^4)-(1/\sigma_n^5\alpha)\tanh(\sigma_n\alpha)} \quad (7)$$

and the pressure gradient is given by:

$$\frac{\mathrm{d}P}{\mathrm{d}z} = \frac{\Delta\mathcal{P}\mu\langle v_z\rangle_u}{(h/2)^2} = \frac{\mu\langle v_z\rangle_u}{2(h/2)^2}\sum_{n=0}^{\infty}\left[\frac{1}{\sigma_n^4} - \frac{1}{\sigma_n^5\alpha}\tanh(\sigma_n\alpha)\right] \quad (8)$$

in which $\sigma_n = (2n+1)\pi/2$, $n = 0, 1, 2, \ldots$ and $\alpha = w_u/h = 7.27$. The solution for $\mathrm{d}P/\mathrm{d}z$ converges rapidly and we use the first 6 terms of the series.

Experimental measurement of the in-plane (x–z plane) velocity profile was achieved using conventional micro-PIV in which the entire profile could be captured in a single field of view. The out-of-plane (y–z plane) velocity profile was obtained point-by-point, by measuring the maximum velocity in the x–z plane and successively stepping the focal plane vertically through the depth of the channel.

In Fig. 6, we compare the axial velocity profiles measured using PIV in the 400 μm × 55 μm straight channel (in both the x–z and y–z planes) with those obtained analytically (Eq. (7)). The close agreement between the experimental and analytical data validates our PIV setup and image processing algorithms.

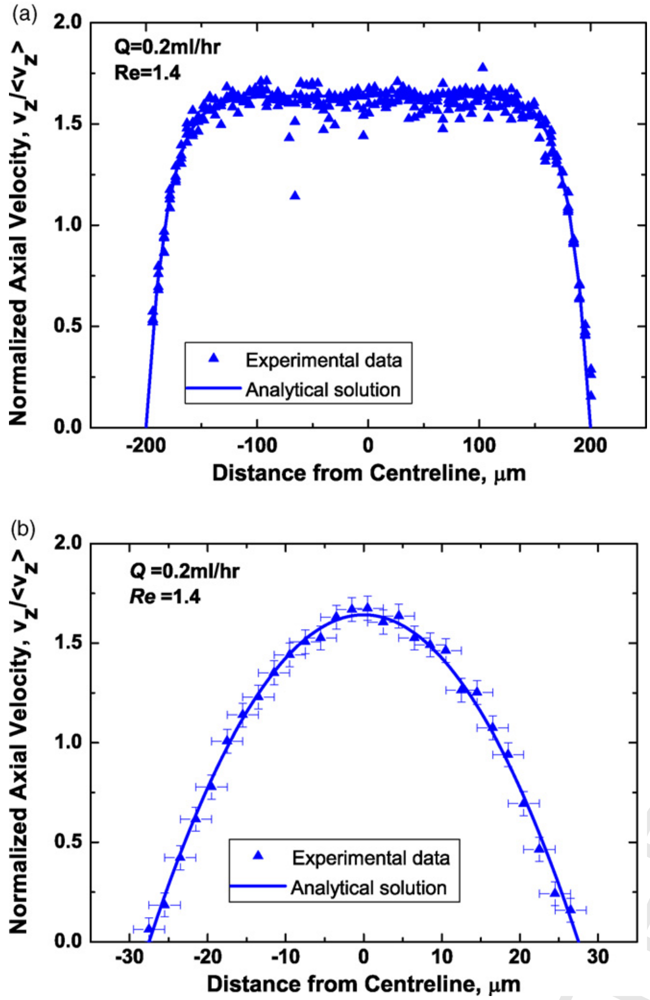

Fig. 6.

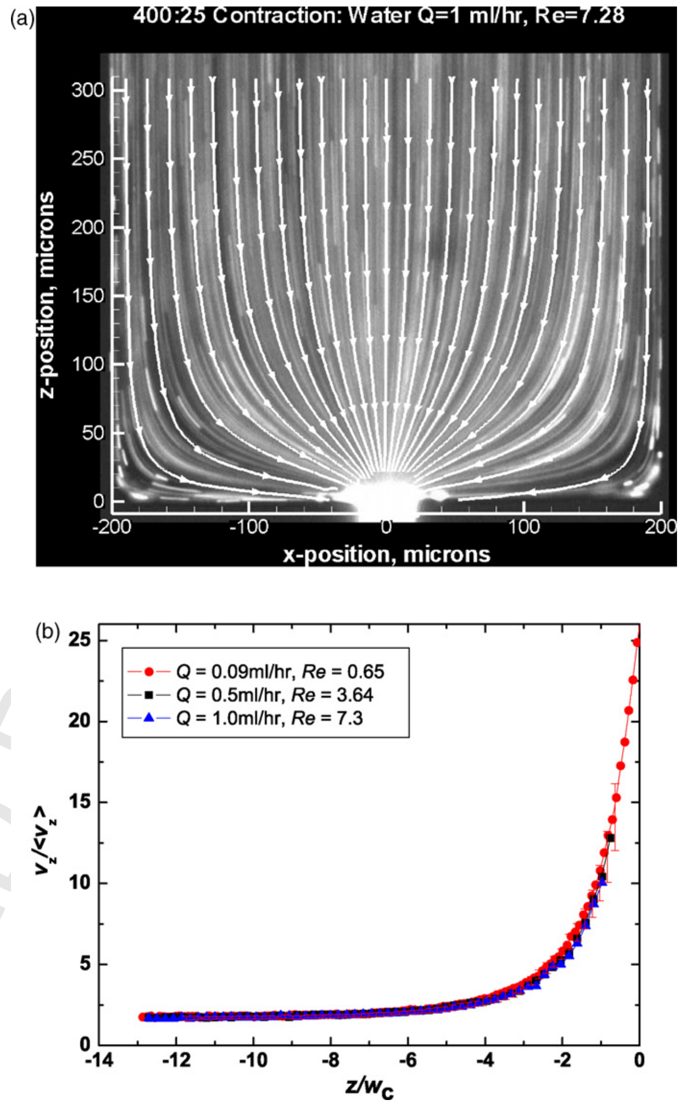

Fig. 7.

3.2.2. *Flow in a 16:1 planar contraction: Newtonian flow*

In Fig. 7a, we compare the streamlines evaluated from the PIV data (using a commercial stream-tracing algorithm in Tecplot) with those obtained through streak imaging for water flowing through a 16:1 contraction at a Reynolds number, $Re = 7.3$ ($Q = 1$ ml/h). For a steady flow, the velocity field $\{v_z(x, z), v_x(x, z)\}$ determined using μ-PIV can also be converted into a set of streamlines (strictly pathlines) using a pathline integration technique. Fig. 7 illustrates the excellent agreement between the two techniques, regardless of the particle size used in each case (0.5 μm for PIV and 1 μm for streak imaging).

Typical axial velocity profiles of a Newtonian fluid (water) traveling along the centerline towards an abrupt 400:26 contraction are presented in Fig. 7b for a range of flowrates, 0.09 ml/h $< Q <$ 1 ml/h ($0.65 < Re < 7.8$). The profiles superpose for all flowrates over this range. At positions along the centreline and just upstream of the contraction plane, $-1 < z < 0$, the dimensionless velocity increases approximately linearly with slope $((\delta v_z/\delta z)(w_c/\langle v_z\rangle)) \simeq 10$.

In Fig. 8a, we present lateral velocity profiles of v_z' versus x for the Newtonian fluid, in which v_z' is the dimensionless axial velocity, and x is the distance from the centerline towards the side walls of the channel. The velocity profiles are presented at a number of axial positions ($z = -300$, -200, -100 and -50 μm, illustrating the evolution of the velocity profile as the contraction plane is approached. Because PIV data is discrete and represents the velocity over a quarter of an interrogation region of 32 × 32 pixels, axial velocity profiles are extracted at locations nearest these nominal values. The real locations of these measurement planes are specified in each corresponding figure. At a nominal distance $z = -300$ μm upstream of the contraction plane, the profile is that of fully developed flow in a rectangular channel for an upstream aspect ratio, $\Lambda_u = 1/\alpha_u = h/w_u = 0.14$. The analytical solution for fully developed flow in a 400 μm × 55 μm channel is also shown in Fig. 8a by the solid line.

At locations nearer the contraction plane, $z = -200$ μm, a peak in the z-component of the velocity develops and velocities nearest the side walls of the channel exhibit a negative deviation from the fully developed profile. At this point, fluid elements begin to feel the presence of the contraction. This effect amplifies as the contraction plane is approached ($z = -100$ μm and

Please cite this article in press as: L.E. Rodd et al., Role of the elasticity number in the entry flow of dilute polymer solutions in micro-fabricated contraction geometries, J. Non-Newtonian Fluid Mech. (2007), doi:10.1016/j.jnnfm.2007.02.006

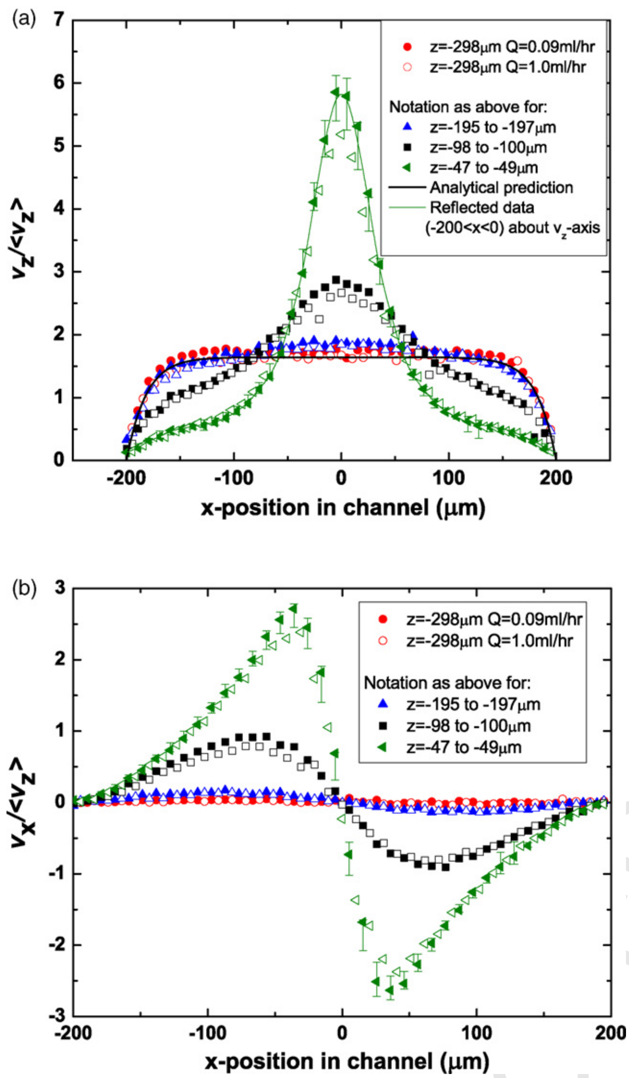

Fig. 8.

$z = -50\,\mu$m). Streamline convergence is also illustrated by the plots of v'_x versus x presented in Fig. 8b, in which non-zero values of v'_x begin to develop at axial positions, $z = -200\,\mu$m and grow as the contraction plane is approached. The symmetry of the flow is elucidated in the plots of v'_x versus x by the reflection in absolute values of v'_x about the centerline axis, $x = 0$.

In accordance with the centerline velocities presented in Fig. 7b, there is little observable difference between the lateral velocity profiles (for both $v'_z(x)$ and $v'_z(z)$) at Reynolds numbers, $Re = 0.65$ and 7.3 ($Q = 0.09$ and 1 ml/h). Error bars corresponding to measurements at $z = -50\,\mu$m have been included in both Fig. 8a and b and indicate the spread of the data for all Newtonian flow conditions.

Small variances in axial position ($z = -46.7\,\mu$m for $Re = 0.65$ and $z = -47.4\,\mu$m for $Re = 7.3$) have been accounted for in the calculated error. The discrepancy in peak velocities may partly be attributed to small obstructions to the flow which result from the lodging of debris or fluorescent particles in the vicinity of the contraction throat. These appear in the raw PIV images as very bright regions, much larger than when observed under transmitted light, and are typically observed only at higher flowrates. They would, however, be expected to cause a local *increase* in the velocity due to an effective reduction in the channel width at the contraction entrance.

3.2.3. *Effect of fluid elasticity*

Having determined the accuracy of our PIV measurements with a Newtonian fluid, we can qualify changes in the velocity fields measured for the four low viscosity elastic solutions, P15G, P30G, P45G and P60G. For brevity, we provide a detailed analysis for fluid P45G, over a range of flow conditions, $0.1 < Re < 1.3$, $2 < Wi < 24$, corresponding to flowrates, 0.1 ml/h $< Q <$ 1.2 ml/h. Summaries of the results for all fluids will be presented in following sections.

In our previous work [2], we demonstrated that the primary effect of fluid elasticity in micron-scale contraction flows was the generation of complex flow structures upstream of the contraction plane at moderate to high Weissenberg numbers, and the dampening of downstream vortices arising from fluid inertia. In the present work, we observe the same effects of fluid elasticity, however with the use of micro-PIV, it is possible to quantitatively assess the progressive changes in the velocity field that occur as the flow transitions between the Newtonian-like, steady viscoelastic, inertio-elastic, and diverging flow regimes.

3.2.3.1. Steady flow: transition from Newtonian-like to steady viscoelastic flow. In Fig. 9, we present the streak images and PIV streamlines upstream of the contraction plane for fluid P45G at flow conditions corresponding to Newtonian-like (Fig. 9a), steady viscoelastic (Fig. 9b), and diverging flow (Fig. 9c). For steady and stable flows (such as the first two cases), smooth and nearly complete PIV vector maps could be achieved using an ensemble average of 25 image pairs. This procedure was less successful for diverging flow regimes, in which the flow is unstable and ensemble averaging could not be implemented. Consequently, blank regions in the velocity field hindered the construction of streamlines without the use of interpolation filters.

Fig. 10a and b illustrate the evolution in centerline velocity profiles for fluid P45G, in terms of the dimensionless variables, v'_z and $\zeta = z/w_c$, corresponding to the Newtonian-like and steady viscoelastic flow regimes. At low values of the Weissenberg number, $Wi < 4$ ($Re < 0.22$, $Q < 0.2$ ml/h), the axial velocity profile at the centerline exhibits Newtonian-like behaviour. Beyond a critical Weissenberg number, $Wi > 4$, the centerline velocity profile exhibits a *delayed* fluid acceleration in regions nearest the contraction throat. As a result, an inflection in the velocity profile appears at approximately $\zeta \cong -2.5$, and at a dimensionless axial velocity, $v'_z \cong 4.5$, consistently for all flowrates corresponding to $4 < Wi < 7$ (0.2 ml/h $< Q <$ 0.35 ml/h, $0.22 < Re < 0.38$). At first, this may appear to be an inertially induced phenomenon; however the velocity profiles in Fig. 7 confirm that the same inflection in the velocity profile is not observed for a Newtonian fluid at the same Reynolds number. Furthermore, numerical simulations for a Newtonian fluid indicate that this behaviour is not observed for Reynolds numbers as high as $Re = 218$ in the absence of fluid elasticity [43]. Analysis

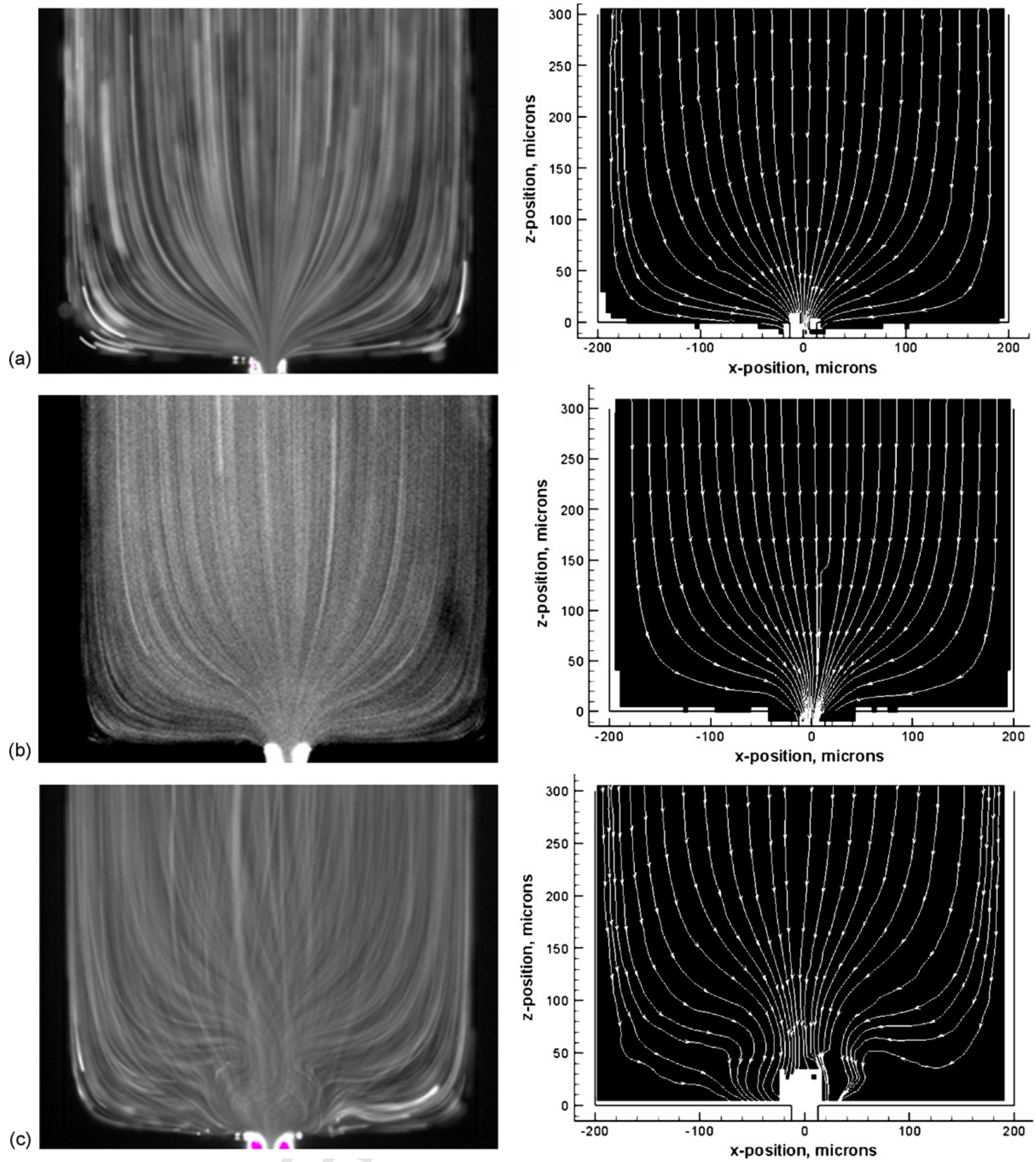

Fig. 9.

of the streak images in Fig. 9 indicate that this effect is a hallmark of steady viscoelastic flow in the contraction region. The departure from Newtonian flow is clearly illustrated in Fig. 10b, which displays the common inflection point for all profiles, and the increased degree of flattening that occurs with higher flowrates.

At low flowrates, $Q = 0.1$ ml/h ($Re = 0.11$, $Wi = 2$), both lateral velocity profiles, $v'_x(x)$ and $v'_z(x)$ for fluid P45G are similar to those observed for Newtonian flow presented in Fig. 8, at all upstream positions, $-300\,\mu\text{m} < z < 0\,\mu\text{m}$. At higher flowrates ($0.1\,\text{ml/h} < Q < 0.35\,\text{ml/h}$) we observe progressive changes in the lateral velocity profiles (particularly in $v'_z(x)$) which reflect the "flattening" of the centerline velocity profile in the region $-2 < \zeta < 0$ depicted in Fig. 10. At $z = -100\,\mu\text{m}$, the peak in the normalized axial velocity increases as the flowrate is increased, while at $z = -50\,\mu\text{m}$, the peak velocity decreases.

3.2.3.2. Time-dependent flow: transition to diverging flow. Following the onset of diverging flow, $Q > 0.35$ ml/h ($Wi > 7.02$, $Re > 0.38$), the flow becomes unstable and time-dependent. This is indicated by the reduced coherence of the streak lines in Fig. 9c, which accompanies diverging flow. The time-dependent nature of the flow field in the diverging flow regime is illustrated in Figs. 11a and b, which were acquired successively at $t = 0$ s and $t = 0.4$ s. These images illustrate the instantaneous structure of the flow field following the onset of an instability.

Please cite this article in press as: L.E. Rodd et al., Role of the elasticity number in the entry flow of dilute polymer solutions in micro-fabricated contraction geometries, J. Non-Newtonian Fluid Mech. (2007), doi:10.1016/j.jnnfm.2007.02.006

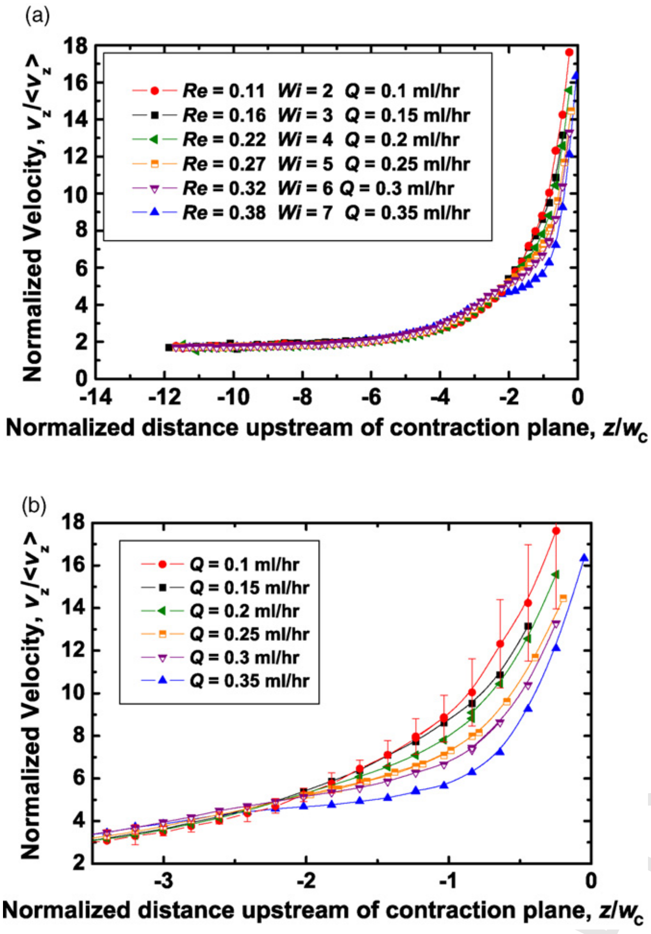

Fig. 10.

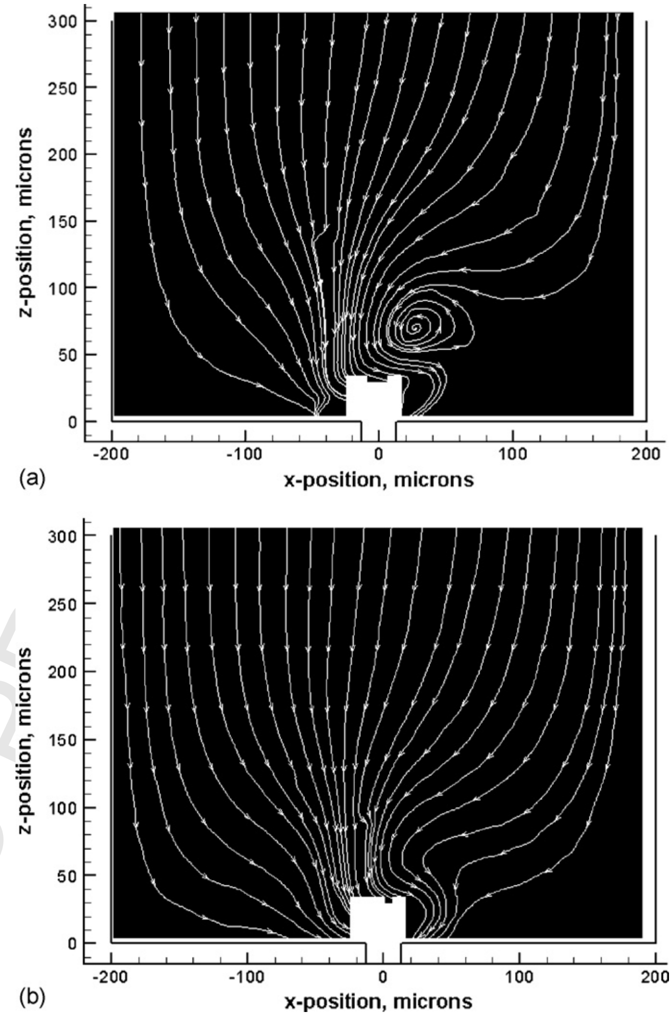

Fig. 11.

The dynamics and structure of diverging flow were characterized according to the “degree of divergence” (spatial characteristics) in the flow and the “amplitude of fluctuation” (temporal characteristics). Firstly, we consider the spatial characteristics of diverging flow. The degree of divergence is manifested in the shape of the axial velocity profile at the centreline. The centerline velocity profile is only meaningful when the flow is symmetric, and since the diverging flow is unstable and time-dependent, it was necessary to isolate instantaneous PIV vector maps in which the flow was symmetric (such as the flow illustrated in Fig. 9c).

The centreline velocity can then be extracted from these images as shown in Fig. 12. This figure illustrates the evolution of the centerline velocity profile in fluid P45G upstream of the contraction plane, as the flowrate increases from $Q = 0.4$ ml/h to $Q = 0.9$ ml/h. The velocity profile corresponding to the initial Newtonian-like flow ($Q = 0.1$ ml/h) is also included for reference. In the diverging flow regime, streamlines diverge away from the centerline upstream of the contraction and then re-converge just prior to entering the contraction throat (see Fig. 9c). In order to conserve mass locally, fluid elements traveling along the centerline must decelerate as adjacent streamlines begin to diverge. As a result, a higher “degree of divergence” leads to a smaller value of the minimum centerline velocity. We can therefore use the minimum axial velocity as one measure of the degree of divergence. Another quantity which can be used to characterize this behaviour is the location of the “bottleneck” just upstream of the diverging streamlines. This can also be identified in the centerline velocity profile as the location of the maximum velocity in the region immediately upstream of

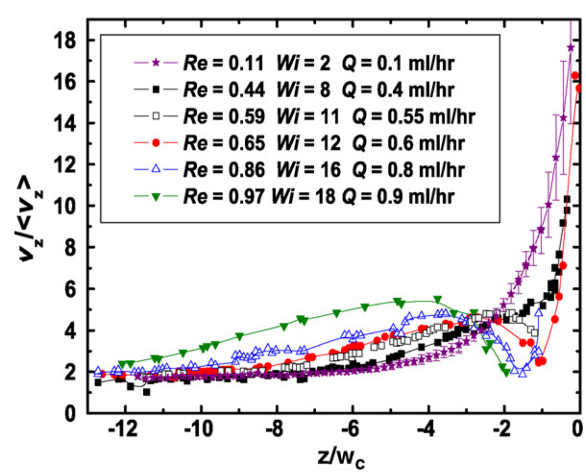

Fig. 12.

diverging streamlines. As the flowrate increases, the position of maximum velocity shifts further upstream and the minimum centreline velocity reduces.

The axial velocity curves are numerically integrated for each value of z, in order to quantify an effective measure of the in-plane flowrate, represented by $A_z = \int_{x=-200}^{x=200} v_z'(x)\,dx$. The integral A_z is calculated for each z-position and for a range of flowrates just prior to and following the onset of diverging flow, $0.35\,\mathrm{ml/h} < Q < 0.6\,\mathrm{ml/h}$ ($7 < Wi < 12$, $0.38 < Re < 0.65$). As we also observed for steady viscoelastic flows, the value of A_z progressively reduces as $\zeta \to 0$, suggesting that fluid elements are moving away from the centreplane in the y-direction; i.e. the flow near the contraction plane is increasingly three-dimensional. As the flowrate is increased, the departure from locally two-dimensional flow (at the centreplane) becomes more pronounced and develops at locations further upstream. For flowrates, $Q > 0.55\,\mathrm{ml/h}$ ($Wi > 11$), the departure from 2D flow appears to saturate, at which point A_z reduces to ∼50% of the equivalent fully developed value at an axial position, $\zeta = -2$.

3.2.3.3. Unstable flow: characterizing streamline oscillations. Unstable viscoelastic flows were characterized according to the amplitude of the fluctuation. This was evaluated from analysis of the temporal characteristics of the flow field. Here, we define the amplitude of the fluctuation as the magnitude of the maximum sideways displacement from the centreline that the fluid core experiences during the unsteady flow. The location of the core is identified as the x-co-ordinate of the maximum axial velocity, in an arbitrarily chosen plane ($z = -100\,\mu\mathrm{m}$, $y = 0\,\mu\mathrm{m}$). The location of this maximum is most easily identified in regions of high velocity gradients (in the x-direction). In light of this, we have chosen a value of z that coincides with regions in the vicinity of the bottleneck. PIV-generated streak images in Fig. 11 indicate that $z = -100\,\mu\mathrm{m}$ is a suitable choice. The axial velocity profile at this measurement plane, $z = -100\,\mu\mathrm{m}$ was evaluated over a series of 25 images (10 s). By evaluating only the x-positions of the velocity peak in each profile, it was possible to quantify the lateral location of the fluid core as a function of time. The standard deviation of all 25 positions was then used as a measure of the amplitude of the fluctuation. This process was repeated for all flowrates in both stable and unstable flow regimes.

For steady Newtonian-like flow, the value of the dimensionless amplitude of the instability is close to zero (as expected). However, it increases as the flowrate increases beyond $Q = 0.7\,\mathrm{ml/h}$ ($Wi = 14$) and a transition to unstable flow occurs. This behaviour is depicted in Fig. 13. A prominent feature of this figure is the reduction in fluctuation amplitude for $Q > 1.2\,\mathrm{ml/h}$. From streak images, it was found that this coincides with the onset of vortex growth, which assists in stabilizing the position of the central fluid core. For comparison, we also show in Fig. 13 the magnitude of the fluctuation evaluated at a second axial positoin, $z = -150\,\mu\mathrm{m}$. There is only a weak dependence on axial position, particularly in the region of unstable flow, and this indicates the robustness of this measurement.

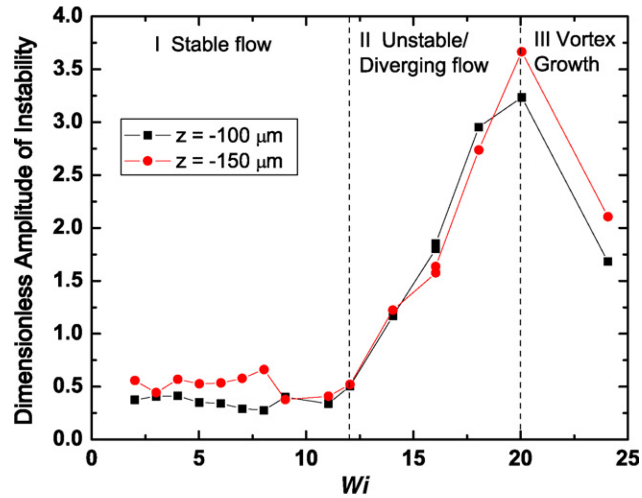

Fig. 13.

3.2.4. The viscoelastic Mach number, Ma

Contour plots of the local viscoelastic Mach number are presented in Fig. 14. The four images correspond to Newtonian-like flow (Fig. 14a), steady viscoelastic flow (Fig. 14b), and the onset of diverging flow (Fig. 14c). For Newtonian-like flow ($Wi = 2.0$), the region nearest the contraction entrance is occupied predominantly by contours of $Ma < 0.3$ (Fig. 14a). The maximum value of the Mach number that occurs in the contraction throat at the center-line (based on a fully developed profile in the contraction) is $Ma_{\mathrm{c\,max}} = 0.7$. As the flowrate is increased ($Wi = 7$) and a transition to steady viscoelastic flow occurs, the region near the contraction entrance experiences higher Mach numbers of approximately $Ma < 0.8$ (Fig. 14b). The maximum value in the contraction throat is $Ma = 2.7$. In this regime, the contours of constant Mach number exhibit a mildly elongated shape, in contrast to the circular-shape contours observed in Newtonian-like flows. The distortion of these circular contours becomes more pronounced in the diverging flow regime as shown in Fig. 14c and d. At the onset of the diverging flow ($Wi = 9$), contours of value $Ma = 0.8$ are easily identifiable upstream of the contraction. The maximum value of the viscoelastic Mach number in the contraction throat is $Ma_{\mathrm{c\,max}} = 3.5$. This general evolution of the flow field is of the same form as described by Hulsen [5], in which large upstream regions of $Ma > 1$ corresponded to the onset of diverging flow for high elasticity solutions ($\epsilon = 0.02$).

3.2.5. Effect of solvent viscosity: the elasticity number

In order to evaluate the effect of changing the elasticity number, we now compare a selection of the kinematic quantities presented above. Firstly, the centerline velocity profiles are presented for each of the elasticity numbers at the same Weissenberg number. This enables a direct assessment of the effects of fluid inertia on the centerline kinematics. Secondly, contour maps of the local viscoelastic Mach number will be presented for each of the fluids at or near the onset of diverging flow. The goal here is to assess the validity of the $Ma > 1$ criterion for the development of diverging streamlines, at different elasticity numbers. Lastly, centerline profiles of the strain rate will be presented for each of

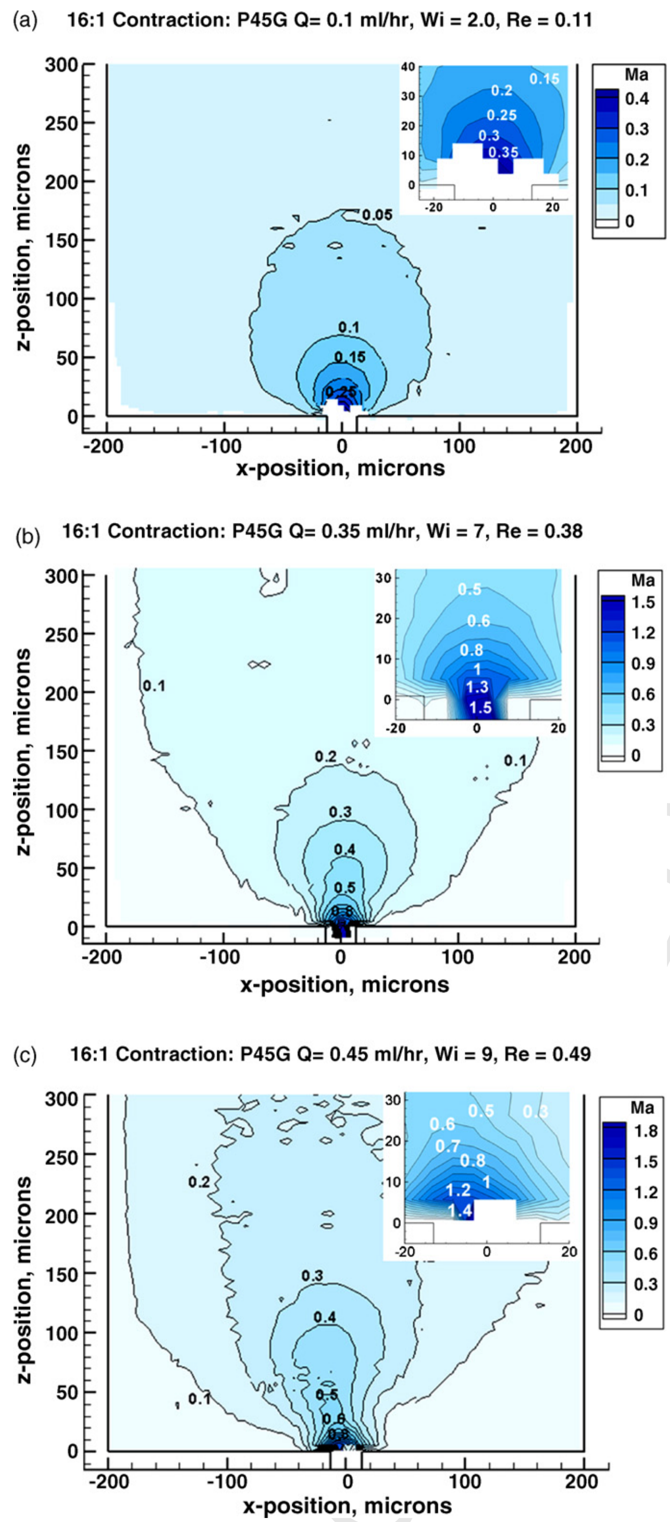

Fig. 14.

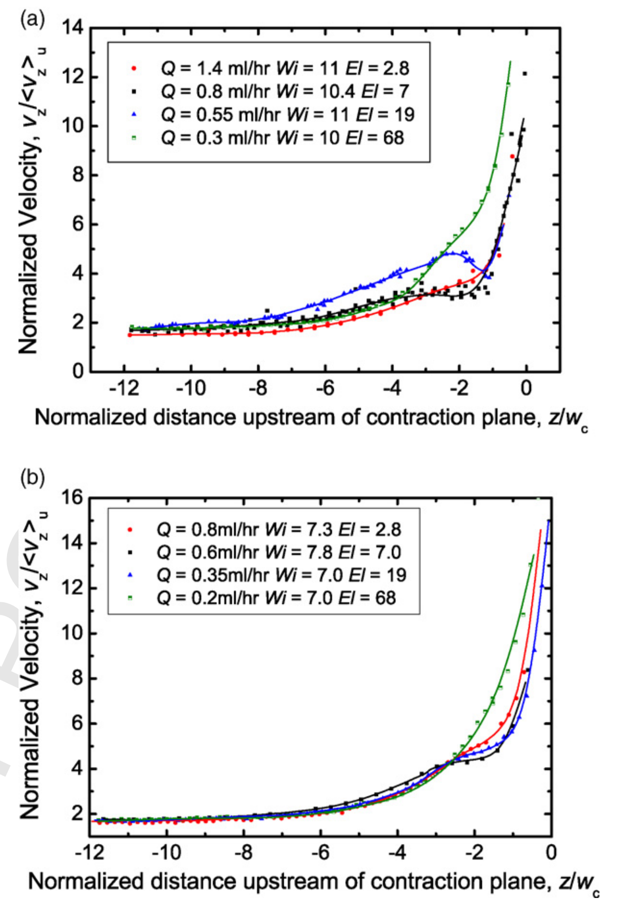

Fig. 15.

the polymer solutions, over the entire range of flow conditions studied in the PIV measurements.

3.2.5.1. Effect of elasticity number on the centerline velocity profile. The centerline velocity profiles for each of the fluids, $El = 2.8$, 7, 19 and 68 are presented in Fig. 15, for Weissenberg numbers, $Wi = 7$, 11. At low Wi ($Wi = 2$), the centerline velocity profile exhibits Newtonian-like characteristics for all elasticity numbers, $2.8 < El < 68$ (such as those in Fig. 7b). At $Wi = 7$ (Fig. 15a), the onset of steady viscoelastic flow is identified by the local inflection of the velocity profile for $2.8 < El < 7$, whilst for the highest elasticity number, $El = 68$, the centreline velocity profile retains Newtonian-like characteristics. The effects of elasticity are most prominent for $El = 7$, and result in a higher normalized velocity upstream of the inflection point, as well as a flatter velocity profile immediately downstream of the inflection point. The higher Weissenberg number for fluid P30G ($Wi = 7.8$, compared with $Wi = 7.0$ for P45G) may be partially responsible for this enhanced elastic effect.

At $Wi = 11$ (Fig. 15b), characteristics of diverging streamlines are observed in the centreline velocity profile for $El = 19$; this is illustrated by the local velocity minimum observed just upstream of the contraction. For $El = 7$, the flat velocity profile near the inflection point suggests the approaching onset of diverging flow, while for $El = 2.8$, the mildly inflected velocity profile indicates that the flow is still steady and viscoelastic in character.

The above information can be summarized in a flow transition map in Wi–Re space, which is presented in Fig. 16. At high elasticity numbers, transitions between flow regimes occur at higher Weissenberg numbers. For moderate elasticity numbers, the critical values of Wi for the onset of flow transitions are lower, however as the elasticity number is further reduced, these val-

Please cite this article in press as: L.E. Rodd et al., Role of the elasticity number in the entry flow of dilute polymer solutions in micro-fabricated contraction geometries, J. Non-Newtonian Fluid Mech. (2007), doi:10.1016/j.jnnfm.2007.02.006

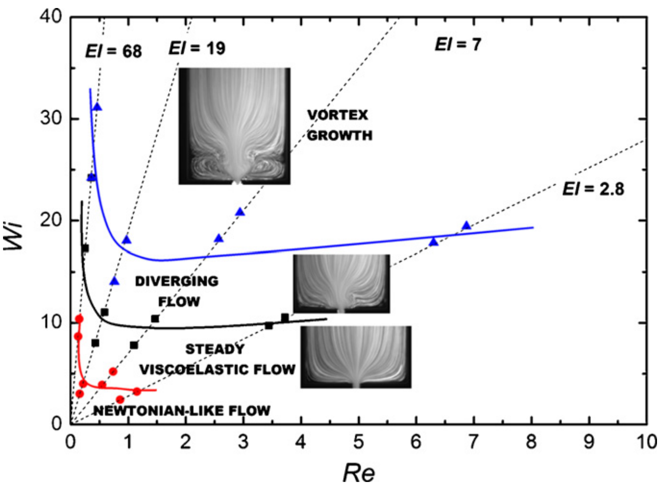

Fig. 16.

ues increase slightly. This implies the existence of a minimum in the boundary between flow regimes, which coincides approximately with our experiments for the P45G fluid with $El = 19$. These results agree qualitatively with observations made in previous numerical and experimental works (Table 1, and Table 1 of [2]); the generation of vortices and other viscoelastic effects are retarded by very high elasticity numbers (e.g. planar flows of Boger fluids [12]) and develop due to an interplay of elasticity and fluid inertia. Furthermore, a Reynolds number that is too large dampens the effects of viscoelasticity, and in particular, inhibits the growth of elastic upstream vortices.

3.2.5.2. Diverging flow and the viscoelastic Mach number; effect of El. Fig. 17a–d show contour plots of the viscoelastic Mach number for each of the four solutions near or at the onset of diverging flow. The corresponding flow conditions for each of the sub-figures are (a) $El = 2.8$, $Wi = 11$, (b) $El = 7$, $Wi = 10$, (c) $El = 19$, $Wi = 11$, and (d) $El = 68$, $Wi = 24$. For $El = 7$, 19 and 68, the onset of diverging flow concincides with a local Mach number, $Ma = 0.8$, in a region just upstream of the contraction plane in the vicinity of the diverging streamlines. However, for the least elastic solution ($El = 2.8$), the equivalent value of Ma is much larger. For example, in Fig. 17a, the local values of the Mach number upstream of the contraction plane are as high as 1.6, yet diverging flow is still absent. This result supports the assertion of Hulsen, in that large values of the Mach num-

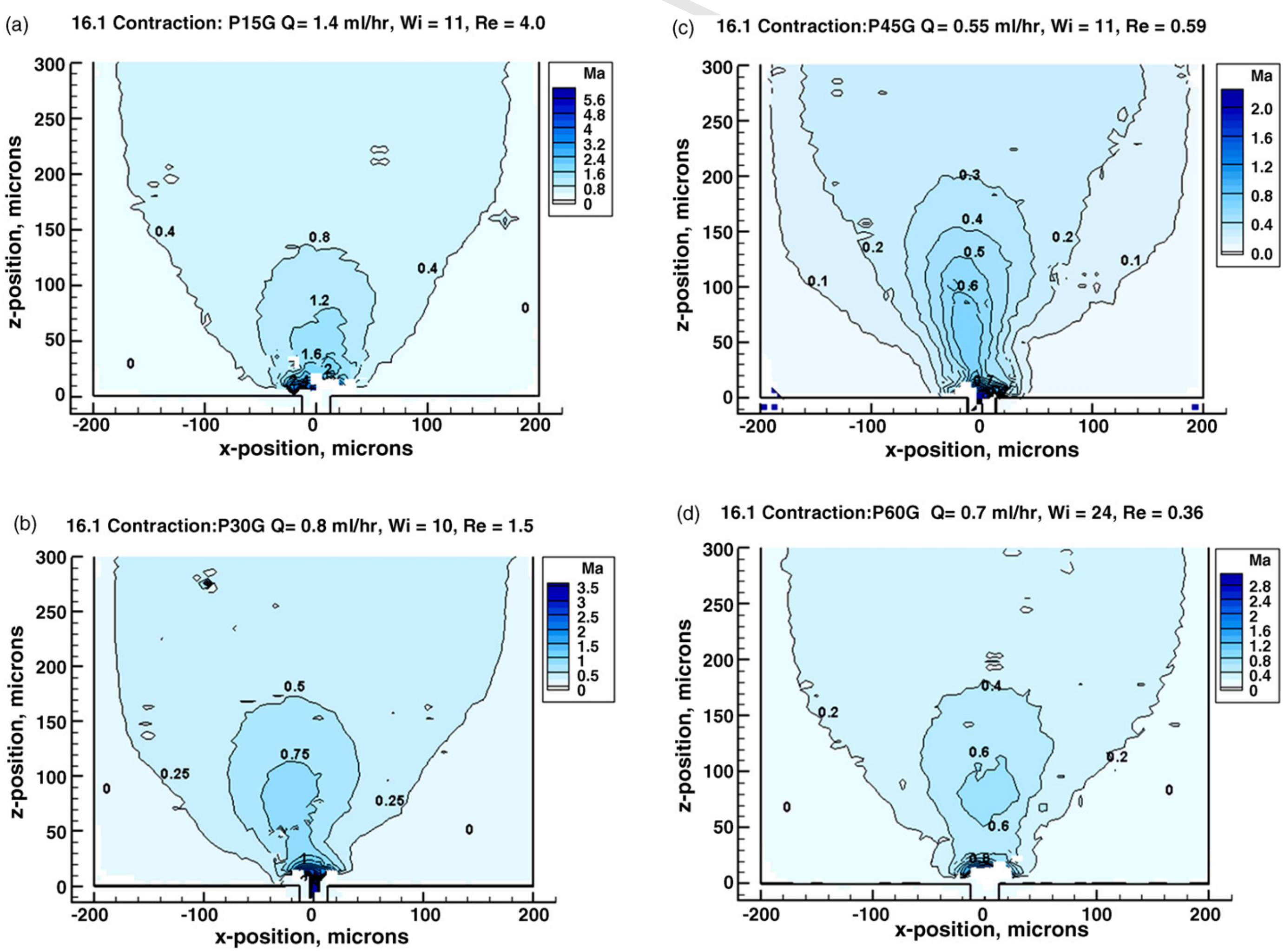

Fig. 17.

Please cite this article in press as: L.E. Rodd et al., Role of the elasticity number in the entry flow of dilute polymer solutions in micro-fabricated contraction geometries, J. Non-Newtonian Fluid Mech. (2007), doi:10.1016/j.jnnfm.2007.02.006

ber do not explicitly lead to diverging flow and that the critical value of the Mach number is not the only important parameter in predicting the onset of diverging flow in polymer solutions with significant solvent viscosities. Furthermore, Hulsen finds that the presence of diverging flow (at $Ma \cong 1$) is only true for high elasticity solutions ($\epsilon = 0.02$), which also agrees with our observations.

3.2.5.3. Centreline strain rate profiles; the onset of elasticity. Similar to the inflection observed in the centreline velocity profile in Figs. 12 and 15, the evolution of the centreline strain rate may also be used to identify the effects of fluid viscoelasticity. Furthermore, values of the strain rate may be used to determine the local values of the Deborah number, $De = \dot{\epsilon}(z)\lambda$ in which λ may be a theoretical Zimm time or a CaBER-determined relaxation time. By evaluating the centreline strain rate using centreline velocity data ($\dot{\epsilon} = \delta v_z/\delta z$), it was found that the maximum strain rate, $\dot{\epsilon}_{max}$ occurs just upstream of the contraction plane. By incorporating the Zimm time, we find that the onset of viscoelastic effects corresponds closely to a value of $De_{max} = 1$ for fluids P15G, P30G and P45G. For fluid P60G, values of De_{max} are greater than unity for all flow conditions, including those in which Newtonian-like behaviour is observed. This is consistent with Fig. 16 which illustrates that the onset of viscoelastic effects occurs at a higher Weissenberg number for fluids with high viscosities and high elasticity numbers (e.g. $El = 68$). The correlation between $De_{max} > 1$ and the onset of fluid elasticity for the other three fluids, however, supports our choice of the Zimm time as the most suitable timescale for characterizing these viscoelastic flows. Furthermore, it was found that the ratio of the maximum strain rate and the downstream shear rate, $\dot{\epsilon}_{max}/\dot{\gamma}_c \cong 0.4$–$0.5$, was found to be approximately consistent between all flowrates and for all elasticity numbers. Since the maximum axial strain rate on the centreplane and the downstream shear rate are of the same order of magnitude, both may be considered equally suitable quantities for calculating the characteristic Weissenberg number (or Deborah number) in this geometry.

3.3. Pressure drop measurements

Pressure measurements were validated in a rectilinear channel flow using a similar procedure to that used for the validation of PIV vectors. In contrast to the PIV measurements, a second rectangular channel with a smaller cross-section and without a contraction–expansion was used. The smaller channel cross-section (55 μm × 57 μm) was chosen in order to achieve larger (and thus more readily measureable) total pressure drops than could be attained in the corresponding 400 μm × 55 μm channel. Fig. 18 illustrates the differential pressure drop measured over a 6 mm section of the rectangular channel with dimensions 55 μm × 57 μm. Again, the experimental pressure measurements show very close agreement with the analytical solution (Eq. (8)). Discrepancies between the data and the analytical solution at high pressure drops ($\Delta P_{12} > 35$ kPa) are a result of the upper limit of the nominal range of the pressure sensor (0–5 psi).

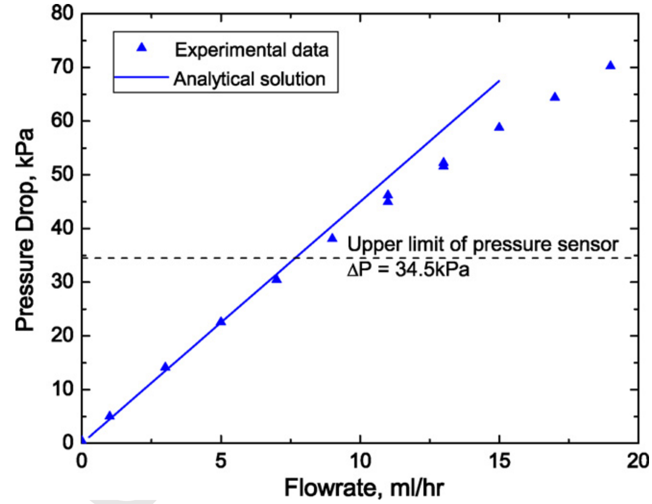

Fig. 18.

In Fig. 19a we present measurements of the total pressure drop in water and the four elastic solutions flowing through the 16:1 contraction. Numerical predictions of the pressure drop for a Newtonian fluid through the same 16:1 contraction–expansion

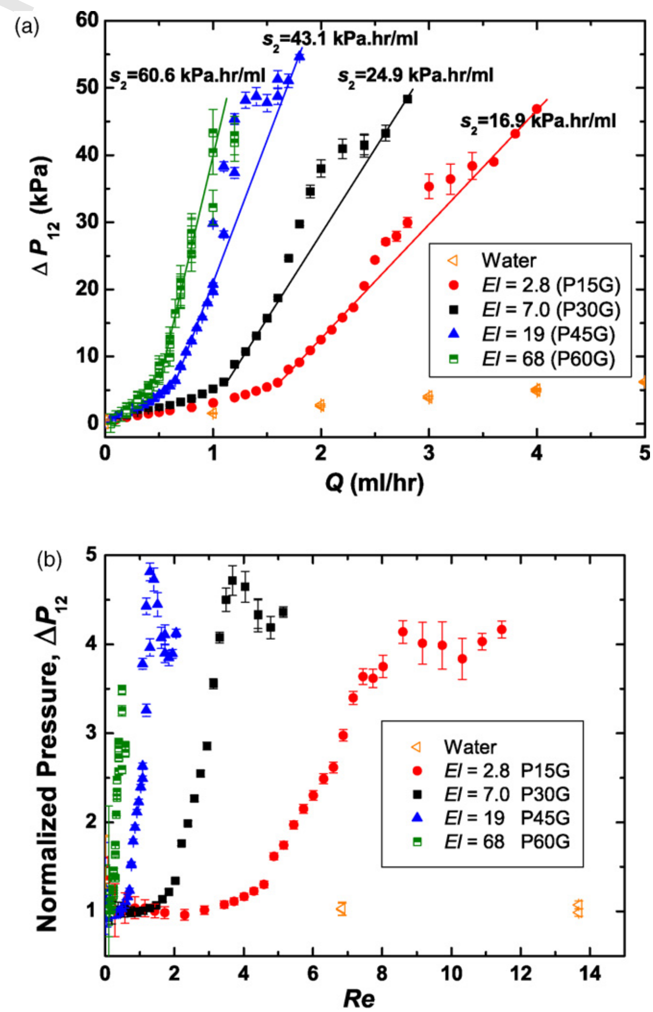

Fig. 19.

geometry can be found elsewhere [43], and agree closely with the experimental data presented here. The pressure drop/flowrate curves for the P15G, P30G and P45G fluids show similar characteristics. At low flowrates, the differential pressure drop ΔP_{12} is linear with Q, and follows the expected behaviour for a Newtonian fluid. The slopes of the curve in this region, $s_1 = \lim_{Q\to 0} \mathrm{d}\Delta P_{12}/\mathrm{d}Q$, for each of the PEO solutions (P15G, P30G, P45G and P60G) are 2.66, 3.78, 7.43 and 13.0 kPa h/ml, respectively. At a critical flowrate (whose value depends on the elasticity number), the slope increases abruptly, corresponding to the onset of viscoelastic effects. In this second region, the slope, maintains a constant value of $s_2 = 16.9$, 24.9, 43.1, and 60.6 kPa h/ml in order of increasing elasticity number, respectively. At higher flowrates again, the measured pressure drop deviates from the previous region of constant slope, resulting in a local shoulder in the ΔP_{12}–Q curve. This final transition is observed only for $El = 2.8$, 7.0 and 19 and corresponds to the onset of unstable vortex growth. At higher flowrates, the large elastic vortices restabilize and undergo steady upstream growth, which results in a third linear region in the ΔP–Q curve. Note that the value of s_2 in the constant slope regions on either side of the shoulder are the same. The flow characteristics in the two regimes that lead to non-linear viscoelatic effects have similar contributions to the total pressure drop. Streak images from the corresponding experiments also indicated that the flow field was symmetric in both regimes, and in the case where the flow was unstable (diverging flow), the *time-averaged* configuration of the flow field was also symmetric. This is in contrast with the unstable vortex growth regime, in which the flow remains largely asymmetric due to the presence of bi-stable vortices.

In Fig. 19b, we replot the data in terms of the dimensionless pressure drop ΔP as a function of Reynolds number, for elasticity numbers, $El = 0$, 2.8, 7.0, 19 and 68. For the Newtonian fluid ($El = 0$), the dimensionless pressure drop has a constant value, $\Delta\mathcal{P} \cong 1$ for Reynolds numbers, $Re < 40$. Although not shown here, the dimensionless pressure drop for water increases to values above unity for $Re > 40$; this is a result of entrance and exit losses (which scale as ρV^2), and become significant at high Reynolds numbers. At $Re = 68$, the dimensionless pressure drop for water reaches a value of $\Delta P = 1.13$. However, since all experiments with the PEO solutions were performed at $Re < 12$, such purely inertial contributions to the extra pressure drop are not expected and the increase in the pressure drop arises from viscoelasticity.

In Fig. 19b, the presence of the shoulders noted previously appear as peaks in the dimensionless pressure drop. The value of the peak pressure drops are $\Delta\mathcal{P}_{\mathrm{peak}} = 4.14$, 4.71 and 4.81, for P15G, P30G and P45G, respectively. There is no observable peak in the curve for the most elastic solution, P60G, however only a limited range of flowrates beyond the inception of vortex growth (0.9 ml/h < Q < 1.2 ml/h) was tested. Streak images corresponding to this range of flowrates, did however suggest that in this high elasticity fluid the viscoelastic vortices were significantly more stable and symmetric, even during the early stages of vortex growth. This may explain the lack of shoulder in the ΔP–Q curve, which appears to accompany a transition to an unsteady flow with fluctuating corner vortices.

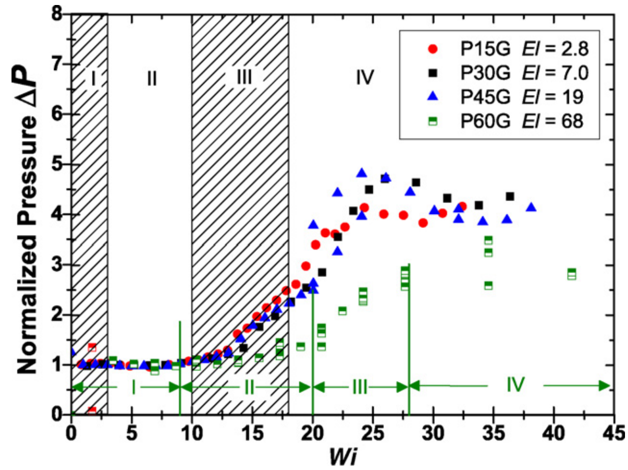

Fig. 20.

In Fig. 20, the dimensionless pressure drop is presented as a function of the Weissenberg number. For the three lowest elasticity numbers, the evolution of $\Delta\mathcal{P}$ with Weissenberg number approximately superimpose, particularly at the onset of elastic effects, corresponding to $\Delta\mathcal{P} > 1$ and in the region of the unstable vortex shoulder. In this figure, four regions have been labelled and correspond to (I) Newtonian-like flow, (II) steady viscoelastic flow, (III) diverging flow (3D, time-dependent flow), and (IV) vortex growth regimes, which have been described in the PIV and streak image results. It was found that steady viscoelastic flow corresponds to a region of $\Delta\mathcal{P} = 1$, i.e., the progressive development of a steady viscoelastic flow field does not incur a measureable extra pressure drop. The first effects of viscoelasticity in this planar contraction flow are thus quite weak and only lead to small changes in the streamline patterns and an inflection point in the centreline velocity (see Figs. 9b and 10). The onset of diverging streamlines (region III) at higher Wi, is however accompanied by an increase in the dimensionless pressure drop, $\Delta\mathcal{P} > 1$. In region IV, $\Delta\mathcal{P}$ continues to increase as a result of the progressive growth in the size of the unstable vortices. Under conditions of steady imposed flowrate in this region, vortices were observed to continuously form and collapse, resulting in a shark-tooth waveform in the transient pressure response. The region following the shoulder corresponds to steady vortex growth, during which the elastic corner vortices no longer grow and collapse.

For the highest elasticity number, $El = 68$, the onset of each of the four regions (I–IV) occur at higher Weissenberg numbers, compared with the other three solutions. For each solution, $\Delta\mathcal{P}$ appears to approach a plateau value for $Wi \to \infty$. For $El = 68$, $\Delta\mathcal{P}_{Wi\to\infty}$ appears to approach a value of $\cong$ 3–4, which is lower than the asymptotic value for the other three less-elastic solutions ($\Delta\mathcal{P}_{Wi\to\infty} \cong$ 5–6). This discernable difference in the magnitude of $\Delta\mathcal{P}$ confirms that the contrasting behaviour observed in PIV and streak images for the highest elasticity number polymer solution is not merely a consequence of a choice in the relaxation time (this affects Weissenberg number only), but is also manifested in the resulting dynamics.

Please cite this article in press as: L.E. Rodd et al., Role of the elasticity number in the entry flow of dilute polymer solutions in micro-fabricated contraction geometries, J. Non-Newtonian Fluid Mech. (2007), doi:10.1016/j.jnnfm.2007.02.006

4. Conclusions

The primary purpose of this work was to explore the role of the background solvent viscosity on the planar entry flow of dilute polymer solutions, corresponding to Elasticity numbers, $2.8 < El < 68$. This was achieved using micro-fabricated contraction geometries and dilute solutions of polyethylene oxide in glycerol/water mixtures. Each fluid exhibited behaviour corresponding to flow regimes which have been identified as (i) Newtonian-like flow, (ii) steady viscoelastic flow, (iii) diverging flow and (iv) elastic corner vortex growth (both unstable and stable). These regimes were identified through streak images, μ-PIV measurements and pressure drop measurements.

A change in the shape of the streamlines upstream of the contraction at low Weissenberg numbers (corresponding to steady viscoelastic flow) was demonstrated to be a result of fluid elasticity because no change in the centreline velocity profile was observed in a Newtonian fluid at corresponding Reynolds numbers or even at an order of magnitude higher. These subtle viscoelastic changes in the centreline velocity profile, however, did not lead to a measureable extra pressure drop; an increase in the dimensionless pressure drop above unity was only observed for higher flowrates following the onset of diverging flow.

The instantaneous structures of three-dimensional unstable viscoelastic flow upstream of the contraction plane were resolved using μ-PIV. As expected, the degree of three-dimensionality was found to increase with increasing Weissenberg number, and flow appeared to be directed *away* from the centreplane. This unstable flow was characterised by the amplitude of the fluctuations in the axial velocity which increased with increasing Weissenberg number. The successive growth and collapse of the elastic corner vortices at high Weissenberg numbers resulted in shark-tooth oscillations in the instantaneous pressure traces and a shoulder in the dimensionless time-averaged pressure drop curve. The decrease in the amplitude of the velocity and pressure drop fluctuations at very high Weissenberg number correspond to a restabilization of the flow and progressive upstream elastic vortex growth.

These results can be summarized in a flow transition map that can be best represented in *Wi*–*Re* space (Fig. 16). This map illustrates that the critical flowrates vary with both *Re* and *Wi* and correspond to a higher Weissenberg number for the highest elasticity number, $El = 68$. For lower elasticity numbers, the transition between flow regimes is a weak function of *El*, such that transitions occur at marginally higher Weissenberg numbers with decreasing elasticity number. This non-linear interaction between inertial and elastic effects helps rationalize previous work, in which Boger fluids (which correspond to high elasticity numbers) only exhibited weak viscoelastic effects [12], and low elasticity number contraction flows failed to exhibit viscoelastic effects due to the overwhelming effects of fluid inertia.

Evaluation of the full kinematic field upstream of the contraction plane also showed that the onset of diverging flow cannot be solely represented by a critical local value of the viscoelastic Mach number. For the lowest elasticity number fluid, $El = 2.8$, viscoelastic Mach numbers in excess of one could still be achieved even in the absence of diverging flow. The onset of viscoelastic effects in the upstream flow could be correlated with exceeding a critical strain rate defined by the inverse of the Zimm time. This supports the idea that the Zimm relaxation time of a polymer solution is the appropriate timescale to be used in predicting the onset of viscoelastic effects in viscoelastic entry flow problems. Although the chains do become stretched as they enter a contraction, the total Hencky strain is less than that encountered in capillary breakup experiments.

Our study demonstrates the value of μ-PIV as a tool for understanding and quantifying the kinematic phenomena associated with both steady and unsteady viscoelastic flows at micron-lengthscales. Furthermore, the subtlety of the transitions between successive flow regimes (particularly the progressive development of steady viscoelastic flow), and the three-dimensional nature of the viscoelastic flow that develops at higher Weissenberg numbers, suggest that μ-PIV is the most effective technique for reliably and quantitatively characterizing the kinematics of a complex flow over a wide range of flow regimes. This work has important implications in the design of microfluidics devices (such as lab-on-a-chip devices) in which the fluid being transported is often non-Newtonian. Additionally, this work provides quantitative data which may be used to validate the permformance of constitutive models in predicting three-dimensional planar entry flows in which both fluid elasticity and inertia are important.

Acknowledgements

The authors would like to thank the ARC Discovery Grants Scheme for funding this work. We would also like to thank the Smorgon family for their financial support through the Eric and Anne Smorgon Memorial Award, the University of Queensland and the Particulate Fluids Processing Centre at the University of Melbourne for infrastructure and support. Lastly, we would like to acknowledge instrumentation support from the Schlumberger Foundation and the Institute for Soldier Nanotechnology (ISN) at MIT.

References

[1] A. Groisman, S. Quake, A microfluidic rectifier: anisotropic flow resistance at low reynolds numbers, Phys. Rev. Lett. 92 (9) (2004) 094501-1–094501-4.
[2] L.E. Rodd, T.P. Scott, D.V. Boger, J.J. Cooper-White, G.H. McKinley, The inertio-elastic planar entry flow of low-viscosity elastic fluids in micro-fabricated geometries, J. Non-Newtonian Fluid Mech. 129 (2005) 1–22.
[3] D. James, J. Saringer, Flow of dilute polymer solutions through converging channels, J. Non-Newtonian Fluid Mech. 11 (1982) 317–339.
[4] K. Kang, L.J. Lee, K.W. Koelling, High shear microfluidics and its application in rheological measurement, Exp. Fluids 38 (2) (2005) 222–232.
[5] M.A. Hulsen, Numerical simulation of the divergent flow regime in a circular contraction flow of a viscoelastic fluid, Theor. Comput. Fluid Dyn. 5 (1993) 33–48.
[6] D.D. Joseph, Fluid Dynamics of Viscoelastic Liquids, Applied Mathematical Sciences, vol. 84, Springer-Verlag, New York, 1990.
[7] R. Evans, K. Walters, Flow characteristics associated with abrupt changes in geometry in the case of highly elastic liquids, J. Non-Newtonian Fluid Mech. 20 (1986) 11–29.

[8] R. Evans, K. Walters, Further remarks on the lip-vortex mechanism of vortex enhancement in planar-contraction flows, J. Non-Newtonian Fluid Mech. 32 (1989) 95–105.

[9] K. Chiba, T. Sakatani, K. Nakamura, Anomalous flow patterns in viscoelastic entry flow through a planar contraction, J. Non-Newtonian Fluid Mech. 36 (1990) 193–203.

[10] K. Chiba, S. Tanaka, K. Nakamura, The structure of anmoalous entry flow patterns through a planar contraction, J. Non-Newtonian Fluid Mech. 42 (1992) 323–350.

[11] P. Cable, D.V. Boger, A comprehensive experiental investigation of tubular entry flow of viscoelastic fluids; part i. vortex characteristics in stable flow, AIChE J. 24 (5) (1978) 869–879.

[12] S. Nigen, K. Walters, Viscoelastic contractions flows: comparison of axisymmetric and planar configurations, J. Non-Newtonian Fluid Mech. 102 (2002) 343–359.

[13] T.N. Phillips, A.J. Williams, Comparison of creeping and inertial flow of an oldroyd-b fluid through planar and axisymmetric contractions, J. Non-Newtonian Fluid Mech. 108 (1–3) (2002) 25–47.

[14] J.M. Kim, C. Kim, J.H. Kim, C. Chung, K.H. Ahn, S.J. Lee, High-resolution finite element simulation of 4:1 planar contraction flow of viscoealstic fluid, J. Non-Newtonian Fluid Mech. 129 (2005) 23–37.

[15] P.J. Oliveira, F.T. Pinho, Plane contraction flows of upper convected maxwell and phan-thien-tanner fluids as predicted by a finite-volume method, J. Non-Newtonian Fluid Mech. 88 (1999) 63–88.

[16] M.A. Alves, F.T. Pinho, P.J. Oliveira, Effect of a high-resolution differencing scheme on finite-volume predictions of viscoelastic flows, J. Non-Newtonian Fluid Mech. 93 (2–3) (2000) 287–314.

[17] M. Alves, P. Oliveira, F. Pinho, Benchmark solutions for the flow of oldroyd-b and ptt fluids in planar contractions, J. Non-Newtonian Fluid Mech. 110 (2003) 45–75.

[18] M.A. Alves, P.J. Oliveira, F.T. Pinho, Numerical simulation of viscoelastic contraction flows, in: K. Bathe (Ed.), Second MIT Conference on Computational Fluid and Solid Mechanics, Elsevier, MIT, Cambridge, USA, 2003, pp. 826–829.

[19] S. Xue, N. Phan-Thien, R.I. Tanner, Three dimensional numerical simulations of viscoelastic flows through planar contractions, J. Non-Newtonian Fluid Mech. 74 (1998) 195–245.

[20] S. Xue, N. Phan-Thien, R.I. Tanner, Numerical investigations of lagrangian unsteady extensional flows of viscoelastic fluids in 3-d rectangular ducts with sudden contractions, Rheol. Acta 37 (1998) 158–169.

[21] J.P. Rothstein, G.H. McKinley, The axisymmetric contraction–expansion: the role of extensional rheology on vortex growth dynamics and the enhanced pressure drop, J. Non-Newtonian Fluid Mech. 98 (1) (2001) 33–63.

[22] L. Genieser, R.A. Brown, R.C. Armstrong, Comparison of measured centerplane stress and velocity fields with predictions of viscoelastic constitutive models, J. Rheol. 47 (6) (2003) 1331–1350.

[23] L.M. Quinzani, R.C. Armstrong, R.A. Brown, Birefringence and laser doppler velocimetry (ldv) studies of viscoelastic flow through a planar contraction, J. Non-Newtonian Fluid Mech. 52 (1) (1994) 1–36.

[24] L. Quinzani, R. Armstrong, R. Brown, Use of coupled birefringence and ldv studies of flow through a planar contraction to test constitutive equations for concentrated polymer solutions, J. Rheol. 39 (6) (1995) 1201–1228.

[25] G.H. McKinley, W.P. Raiford, R.A. Brown, R.C. Armstrong, Nonlinear dynamics of viscoelastic flow in axisymmetrical abrupt contractions, J. Fluid Mech. 223 (1991) 411–456.

[26] M.A. Alves, Escoamentos de fluidos viscoelasticos em regime laminar, Ph.D. Thesis, University of Porto, 2004.

[27] P. Cable, D.V. Boger, A comprehensive experiental investigation of tubular entry flow of viscoelastic fluids; part ii. the velocity field in stable flow, AIChE J. 24 (6) (1978) 992–999.

[28] P. Cable, D.V. Boger, A comprehensive experiental investigation of tubular entry flow of viscoelastic fluids; part iii. unstable flow, AIChE J. 25 (1) (1979) 152–159.

[29] B. Purnode, M. Crochet, Flows of polymer solutions through contractions. part 1: flows of polyacrylamide solutions through planar contractions, J. Non-Newtonian Fluid Mech. 65 (1996) 269–289.

[30] L.E. Rodd, Planar entry flow of low viscosity elastic fluids in microfabricated contraction geometires, Ph.D. Thesis, The University of Melbourne, 2006.

[31] L.E. Rodd, T.P. Scott, J.J. Cooper-White, G.H. McKinley, Capillary breakup rheometry of low-viscosity elastic fluids, Appl. Rheol. 15 (1) (2005) 12–27.

[32] V. Tirtaatmadja, G.H. McKinley, J.J. Cooper-White, Drop formation and breakup of low viscosity elastic fluids: effects of molecular weight and concentration, Phys. Fluids, in press.

[33] H. Barnes, J. Hutton, K. Walters, An Introduction to Rheology, Elsevier Science Pub. Co., Amsterdam, 1989.

[34] Y. Amarouchene, D. Bonn, J. Meunier, H. Kellay, Inhibition of the finite-time singularity during droplet fission of a polymeric fluid, Phys. Rev. Lett. 86 (16) (2001) 3558–3561.

[35] Y. Christanti, L.M. Walker, Effect of fluid relaxation time of dilute polymer solutions on jet break up due to a forced disturbance, J. Rheol. 46 (3) (2002) 733–748.

[36] R. Prabhakar, J. Prakash, T. Sridhar, Influence of configuration-dependent intramolecular hydrodynamic interaction on elastocapillary thinning and breakup of filaments of dilute polymer solutions, J. Rheol. 50 (6) (2006) 925–947.

[37] C. Clasen, J. Plog, W.-M. Kulicke, M. Owens, C. Macosko, L. Scriven, M. Verani, G.H. McKinley, How dilute are dilute solutions in extensional flows? J. Rheol. 50 (6) (2006) 849–881.

[38] M.E. Mackay, D.V. Boger, An explanation of the rheological properties of boger fluids, J. Non-Newtonian Fluid Mech. 22 (2) (1987) 235–243.

[39] C. Stoltz, J.J. de Pablo, M.D. Graham, Concentration dependence of shear and extensional rheology of polymer solutions: Brownian dynamics simulations, J. Rheol. 50 (137) (2006) 137–167.

[40] S. Wereley, C. Meinhart, Micron resolution particle image velocimetry, in: K.S. Breuer (Ed.), Microscale Diagnostic Techniques, Springer-Verlag, New York, 2004.

[41] S. Devasenathipathy, J. Santiago, C. Meinhart, S. Wereley, K. Takehara, Particle imaging techniques for microfabricated fluidic systems, Exp. Fluids 34 (4) (2003) 504–514.

[42] F.M. White, Fluid Mechanics, fifth ed., McGraw-Hill, New York, 2003.

[43] M. Oliveira, L.E. Rodd, G.H. McKinley, M.A. Alves, Simulations of extensional flow in microrheometric devices, in press.

Please cite this article in press as: L.E. Rodd et al., Role of the elasticity number in the entry flow of dilute polymer solutions in micro-fabricated contraction geometries, J. Non-Newtonian Fluid Mech. (2007), doi:10.1016/j.jnnfm.2007.02.006